RESEARCH ARTICLE | NOVEMBER 06 2025

Blade shape evaluation for cross-flow tidal turbines—A fast and automated assessment tool for early design stage based on power and load coefficients

K. Ruiz-Hussmann ; P.-L. Delafin ; T. Bennecke; C. Bonamy ; S. Hoerner

Physics of Fluids 37, 117111 (2025)
https://doi.org/10.1063/5.0291030

Physics of Fluids ARTICLE pubs.aip.org/aip/pof

Blade shape evaluation for cross-flow tidal turbines—A fast and automated assessment tool for early design stage based on power and load coefficients

Cite as: Phys. Fluids **37**, 117111 (2025); doi: 10.1063/5.0291030
Submitted: 15 July 2025 · Accepted: 16 October 2025 ·
Published Online: 6 November 2025

K. Ruiz-Hussmann,[1,2,a)] P.-L. Delafin,[2] T. Bennecke,[1] C. Bonamy,[2] and S. Hoerner[1,2]

AFFILIATIONS

[1]Laboratory of Fluid Dynamics and Technical Flows, Institute of Fluid Dynamics and Thermodynamics, Otto-von-Guericke-University Magdeburg, Universitätsplatz 2, 39106 Magdeburg, Germany
[2]Laboratoire des Écoulements Géophysiques et Industriels, University Grenoble Alpes, Grenoble INP, CNRS, 3800 Grenoble, France

[a)]Author to whom correspondence should be addressed: karla.ruiz@ovgu.de

ABSTRACT

Cross-flow tidal turbines (CFTT) are a promising technology for tidal energy exploitation. They are omni-directional, feature high area-based power density and a simple design. However, due to their rotation around the vertical axis, the blades undergo a continuous change in their angle of attack, leading to alternating loads, which can cause fatigue failure. For this reason, blade loads should already be taken into account in the early design phase. This study presents a standardized and automated method for evaluating the influence of blade profile shapes on power and load coefficients. Fully automated computational fluid dynamics simulations are coupled with an analytical mechanical model, treating blades as a clamped beam. This allows for evaluation of the turbine's performance (power coefficient C_P) and the structural load. A stress coefficient C_σ is introduced to quantify fatigue risk by taking both amplitude and mean stress into account. The methodology is applied to 120 randomized blade shapes with different operating points. Results indicate that a stronger blade cambering reduces C_P, while C_σ remains unaffected. Nevertheless, the blade's chord length and operating point show a weak correlation with C_σ. An additional detailed analysis of four arbitrarily selected cases and the reference case is conducted. The findings highlight the importance of optimized blade geometries to balance the power output and the structural lifetime of CFTTs.

I. INTRODUCTION

Tidal stream turbines have emerged as a promising technology for renewable energy and offer a viable solution for harnessing the hydrokinetic energy of tidal currents, as they can be positioned in the free stream without the need for additional structures. Axial-flow turbines commonly have a horizontal axis aligned with the direction of the flow, and are therefore often referred to as horizontal-axis turbines (HAT). In contrast, cross-flow tidal turbines (CFTT) can operate both in a vertical and horizontal orientation. In consequence, we refer here to CFTT for all turbines that have their rotation axis perpendicular to the flow direction. This feature makes them omnidirectional, as they spin around their axis regardless of the direction of the incoming flow. This makes them particularly suitable for harnessing the energy of alternating tidal currents as there is no need for a yawing system, unlike with axial-flow turbines. Additionally, they are known to have a magnitude higher area-based power density in farm installations when compared to HAT,[1–3] which are dominating the wind energy sector nowadays.

However, despite their advantages, CFTTs also face challenges that limit their full potential, such as their lower single turbine efficiency compared to competing HAT designs.[4–7] Another key challenge is the complex flow pattern in the rotor, which occurs due to the rotation around the vertical axis perpendicular to the flow. Thereby, the turbine blades undergo a continuous change of their angle of attack during each rotation, leading to dynamic stall and flow separation with severe alternating loads on blades and support structure. These loads may result in flow-induced vibrations and dynamic stress that can cause fatigue failure.[8–10] Geng *et al.* found the blade-strut connection

to be the most endangered structural component of vertical axis wind turbines.[11] Consequently, this component can be considered to be most prone to fatigue failure. Kirke *et al.* stated that alternating radial loads can even lead to direct failure of the turbine structure.[6,7] These obvious drawbacks and challenges highlight the necessity to determine a relevant methodology to properly assess the hydrodynamic loads experienced by CFTTs and their impact on the blade support structure at early design stages.

Most literature on CFTTs focuses on modeling the flow around the turbine and improving the rotor efficiency, for example, by increasing the power (C_P) or the torque (C_Q) coefficients, e.g., Refs. 4, 8, 12–17 to name some recent studies. The structural blade loads have been less thoroughly analyzed. A quantification of dynamic blade loads has been discussed in a few publications. Although these studies have considered the forces acting on the turbine, most do not further address or analyze the effect of these forces on the turbine structure.[6,7,10,18,19] A few publications further analyzed load effects on the turbine structure in weak coupled fluid–structure interaction (FSI) studies by mapping the pressure distributions achieved with computational fluid dynamics (CFD) simulations in a finite element analysis (FEA). This allows for a quantification of the stresses experienced by the structure.[12,20–23] Additionally, both Ali *et al.* and Gorgun used this methodology and extended it by the application of the Goodman fatigue theory in order to estimate the fatigue life of the turbine.[20,22]

When extending the literature range from CFTTs to fatigue in tidal stream turbines, it is found that research is predominantly focused on horizontal axis tidal turbines, such as those by Badshah *et al.*,[24] Finnegan *et al.*,[25] de Souza Custódio Filho *et al.*,[26] Gonabadi *et al.*,[27] and Zhang *et al.*[28] Additionally, Walker and Thies[29] reviewed 58 tidal stream energy deployments, regarding their system reliability. They found that the primary cause of failure is blade fatigue, mostly due to underestimation of the blade loading. Although the majority of the studied sites had horizontal axis tidal turbines, this underlines the relevance of understanding and assessing the loads on hydrokinetic turbines in general.

FSI techniques are often employed to calculate material stress in the turbine rotors. Examples are Saeed *et al.*[30] on a Francis runner, Sick *et al.*,[31] and Andolfatto *et al.*[32] on a Pelton turbine runner, Kumar and Sarkar[33] on a Savonious hydrokinetic turbine, Badshah *et al.*[24] on a horizontal axis tidal turbine, Lin *et al.*,[34] and Geng *et al.*[11] on a vertical axis wind turbine.

An analysis of a full turbine runner with this methodology is computationally expensive, and therefore, often only conducted at a late stage of the design process. Several CFD and FEA simulations need to be conducted in order to consider different load cases a turbine may experience. For this reason, Hameed and Afaq[35] predicted the deflection and the stress acting on the blades of a vertical axis wind turbine by using the Euler–Bernoulli beam theory (EBB) for uniformly distributed loads to avoid FEA simulations. Normal force and centrifugal loads acting on the blade are assessed in their study. A similar approach is used by Alerci *et al.*,[36] who calculated the material stress induced at the bucket root of a Pelton turbine runner by simplifying the geometric structure and applying the EBB theory. This analytical approach is by far less computationally expensive than a full scale FEA, and therefore, better suited when comparing a large number of designs and load cases, e.g., during the early-stage design process.

Most commonly in the literature, after calculation of stress, the prediction of the fatigue lifetime is conducted using S–N-curves, also known as the Wöhler curves, combined with a Rainflow counting algorithm and the Palmgren–Miner's rule.[26,37–39] This fatigue analysis allows for the understanding of the fatigue life of structures experiencing cyclic loads. However, the S–N-curves do not account for any static loads, such as centrifugal loads in the runner, which can become relevant when aiming for an increase in the turbine's lifetime. In addition to this approach, it is also possible to apply the Smith diagram, which is derived from several S–N-curves for different loading ranges, combining each of their fatigue strength values into one diagram.[40] In comparison to the S–N-curves, the implementation of the Smith diagram accounts for additional static loads and can alternatively be employed for fatigue life estimation. Therefore, it considers both the mean of the stress values as well as the stress peak amplitude.[41]

It can be summarized that only a few research studies have been conducted on the alternating loads on CFTTs, although they may lead to fatigue failure of the turbine runner. Furthermore, FSI studies followed by a S–N curve assessment can be seen as the current state-of-the-art method for fatigue life analysis. This methodology can become computationally expensive for large structures and is, in consequence, not very suitable for an early-stage design process. In addition, the employment of S–N curves neglects static loads. This article presents a CFD-based assessment of the flow, complemented by an analytical methodology to analyze the fatigue risk from blade loads on different CFTTs blade shapes. Hereby, a dimensionless indicator suitable for the early design stage is introduced. Here, static and alternating loads are condensed into a single value, similarly to the approach presented by Jelaska *et al.*, where the Smith diagram is used for the fatigue life estimation of combined high and low cycle fatigue.[42] The methodology has been developed within a broader project, which aims at improving the performance and reducing the stresses on CFTTs by implementing active blade pitching.

In the following study, we will present a fast and accurate method to assess the loads on the cross-flow tidal turbine's blade support structure by introducing dimensionless indicators to evaluate turbine power and structural loads on the blade support. The methodology is illustrated through the multiphysical analysis of a CFTT equipped with a wide range of blade shapes and different operating points. It provides a structured approach for a cost effective, automatized and systematic assessment of the blade shape impact on performance and lifetime in rotating machinery using open source software and is particularly suitable for the early-stage design process.

II. METHODOLOGY

The evaluation of the fluid–structure interactions and the fatigue risk for a turbine rotor with a large number of possible parameter sets requires automation of the tool chain in use. In the present study, the hydrodynamic forces and moments acting on the turbine blades are obtained from 2D numerical simulations, followed by a post-processing step that evaluates the performance (C_P) and assesses the fatigue risk (C_σ) of each case through a simplified analytical model. Similar to a weak-coupled FSI approach, the CFD results are used to analyze the structural response. However, no solid solver is coupled with the simulations. The complementary steps of the assessment process and their validation are discussed subsequently. Figure 1 shows a flow chart outlining the methodology.

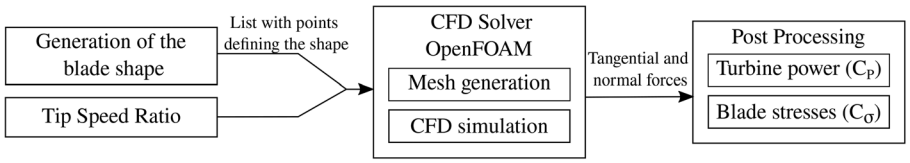

FIG. 1. Flowchart of the presented methodology.

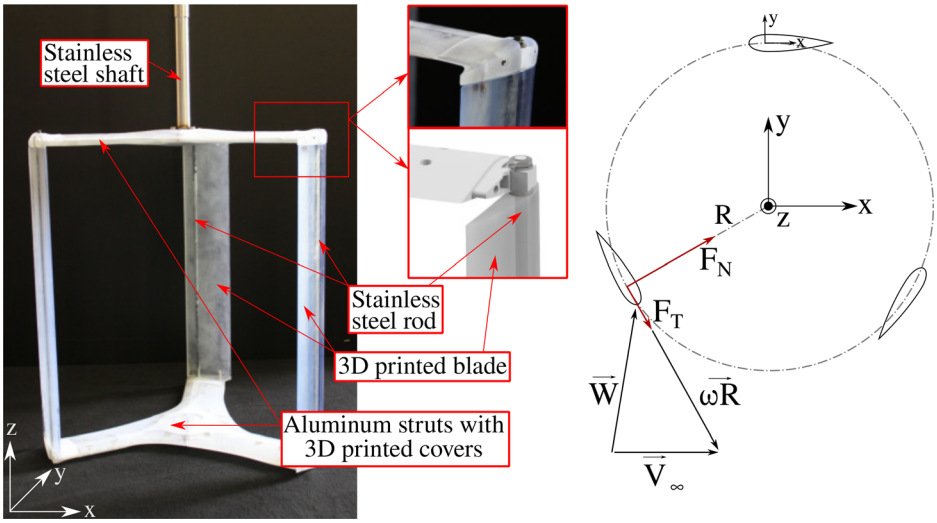

FIG. 2. Left: Flume model of the CFTT analyzed in the present study. The turbine is mounted with an upper and lower shaft, whereby the latter is not shown in the figure. The model is equipped with covers on the blade-support-junctions (detail top). The junction without cover is shown in the 3D CAD render (detail below). Right: Top view of a CFTT with forces and velocity triangle at one blade for an arbitrary rotor angle. The origin of the global coordinate system is positioned at the turbine center, while the local coordinate system of the blade is positioned at the quarter chord position in the x-direction and on the camber line in the y-direction and rotates with the blade around the turbine center.

A. Turbine geometry and blade definition

The turbine geometry corresponds to a three-bladed Darrieus rotor with a diameter and height of 400 mm. It has straight blades which are connected with the upper and lower shaft through aluminum struts at the upper and lower ends of the blades (Fig. 2). The mechanically relevant connection between struts and blades is given by a stainless steel rod (diameter of 12 mm) embedded in 3D printed polymer blades. This rod connects to the metallic inner structure of the struts, which is covered with 3D printed shells. The materials of the different components are labeled in Fig. 2 (left), and their properties are listed in Table I.

The effect of different blade shapes on the power and the loadings on the turbine will be tested. For this reason, a broad range of blade shapes will be created automatically and randomly. A pseudo-randomized Sobol distribution for the generation of the blade parameters has been employed to cover the entire design space.[46] Each blade shape is defined by ten parameters, or points respectively, as shown in Fig. 3 with red stars and blue dots. Two points (red stars) are fixed in their quarter chord position and lead to a predefined thickness of 13 mm, given by the rod positioned inside the blade. The chordwise position of eight points (shown as blue dots) is fixed, but set as a relative function of the chord length. Variables Y0–Y7 define the camber line, and T1–T6 provide the desired profile thickness at this location. The choice of ten node points represents a trade-off between the geometric flexibility and the number of parameters. Iterative testing showed that fewer points would lead to unrealistic blade shapes, while more points would increase the design space excessively without providing additional geometric diversity. The blade has a blunt trailing edge. It is imposed by the intended manufacturing process for the blades using a 3D printed core, which will be wrapped with a carbon fiber sheet with a thickness of 0.23 mm. For this reason, the trailing edge shape consists of two points with a fixed distance of 0.46 mm in the y-direction between them. Therefore, a single parameter defines the leading edge.

Besides the blade shape and its chord length, the operating point of a turbine has great influence on the power and the structural loads on the turbine. The operating point of hydrokinetic turbines is usually defined by the tip speed ratio (TSR), which describes the ratio between the tangential velocity of the turbine blade tips (at maximum radius), given by the angular velocity ω_T multiplied by the turbine radius R, and the velocity of the incoming flow V_∞

TABLE I. Material specifications of the turbine components.[43]

Stainless steel 1.3401 (AISI 304)[43]		
Young's modulus	E	193–200 GPa
Yield strength	R_p	215 MPa
Ultimate tensile strength	R_m	505 MPa
Aluminum Al6061 T6[44]		
Young's modulus	E	68.9 GPa
Yield strength	R_p	276 MPa
Ultimate tensile strength	R_m	310 MPa
Clear Resin V4.1 (post-cured)[45]		
Young's modulus	E	2.4 GPa
Ultimate tensile strength	R_m	53 MPa
Flexural strength	σ	103 MPa

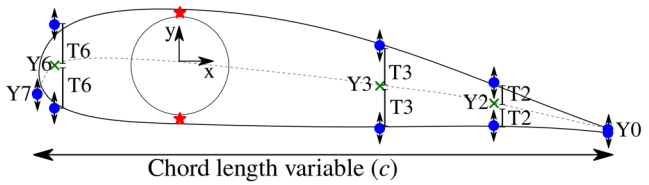

FIG. 3. Definition of the node points that determine the hydrofoil shape. Points marked with red stars are fixed, whereas blue circles are free parameters for individualized blade shapes. The coordinate system represents the local coordinate system of the blade as defined in Fig. 2, located at the quarter chord position in the x-direction and on the camber line in the y-direction. (Adapted from Ruiz-Hussmann *et al.*, Int. Mar. Energy J. **8**, 47–55, 2025.[47] Copyright 2025 Author(s), licensed under a Creative Commons Attribution (CC BY) license.

$$TSR = \frac{\omega_T \cdot R}{V_\infty}. \tag{1}$$

In consequence, the TSR is the tenth parameter of the study, the other nine given by the chord length and the blade points.

To ensure that the blade shape, its chord length, as well as the TSR remain in a suitable range for the application on a CFTT, constraints are set to all design variables before generating the Sobol distribution of the design parameter. The imposed minimal and maximal values for each design parameter are listed in Table II. For the TSR, a range between 1.5 and 3.0 has been defined, and for the chord c, a minimal length of 60 mm and a maximal length of 90 mm is allowed. This is in accordance with the findings from Ref. 48, which investigated the relation between turbine solidity ($\sigma = n \cdot c/R$) and TSR. Here, the best performing turbine featured a TSR of 1.82 and a solidity that corresponds to a chord length of 75 mm in our turbine. Therefore, the chord length and TSR limits (c from 60 to 90 mm, TSR from 1.5 to 3.0) were chosen around these values. Additionally, limits and constraints on the eight variable blade shape points are established to allow only for straight or downwards cambered blades, and a slimming toward the trailing edge was enforced. This ensures a reasonable blade designs for the presented study. The following five design constraints have been imposed:

- $T2 - 0.7 \cdot T3 < 0$
- $Y0 - Y2 < 0$
- $Y2 - Y3 < 0$
- $Y7 - Y6 > 0$
- $Y6 - T6 - Y7 < 0$

TABLE II. Minimal and maximal values of the ten imposed design parameters.

Variable	Minimal value	Maximal value
Tip speed ratio	1.5	3.0
Chord length	60 mm	90 mm
Y0	−10.0 mm	0.0 mm
Y2	−10.0 mm	0.0 mm
Y3	−10.0 mm	0.0 mm
Y6	−10.0 mm	0.0 mm
Y7	−10.0 mm	0.0 mm
T1	2.0 mm	5.2 mm
T2	2.0 mm	5.2 mm
T6	2.0 mm	6.5 mm

In order to provide a more intuitive presentation of the design space of ten parameters, three variables have been derived from the resulting blade shapes. They allow for a more accessible description of the generated profiles:

1. the mean thickness of the blade,
2. the maximal camber, given by the maximal distance between the chord line and the camber line, and finally
3. the tortuosity. It describes the ratio of the length of the camber line l to the chord length c (tortuosity $= l/c$). Typically used to describe the path in porous media, tortuosity in this context defines the deviation of the camber line from a straight line. A tortuosity equal to one describes a symmetrical foil, while higher values indicate twisted or wavy camber lines.

Table III lists the ranges of the three derived variables that describe the profile shape and size in a more convenient manner than the parameters from the design space.

In addition to the automatically generated shapes, a reference case has been introduced: a NACA0018 foil with a chord length of 72.44 mm, whose mean line was projected to the circumference of the turbine. This results in a cambered foil, as presented by Maître *et al.*[49] A TSR of 1.9 was chosen. It had been found from detailed investigations of the characteristic curve of the reference case that it represents the best operating point for the chosen conditions.

B. Numerical methods

After generating the parameter sets in a broad range of profile shapes, sizes, and operating points, parallelized 2D numerical simulations are employed to evaluate each parameter set. Hydrodynamic forces and moments acting on the turbine rotor are calculated. This allows for a detailed analysis of the performance of each design, complemented with an assessment of the hydraulic loads. The numerical tool chain comprises three main parts:

1. the spatial discretization (automated meshing),
2. the actual CFD simulations (data generation) and
3. post processing (evaluation).

In the present work, the open-source *OpenFOAM* toolkit (version 2212 from the ESI fork) is employed, and all simulations were performed at the HPC facility of the Laboratoire des Ecoulements Géophysiques et Industriels (LEGI) in Grenoble, France. The main characteristics and settings of the numerical simulations are summarized in Table IV and further explained in the following sections.

TABLE III. Minimal and maximal values of the variables derived from the different shapes generated.

Variable	Minimal value	Maximal value
Mean thickness	7.7 mm	9.9 mm
Maximal camber	1.12 mm	10.59 mm
Tortuosity	1.00	1.07

TABLE IV. Main characteristics of the numerical setup.

Parameter	Specification
Type	2D URANS, single phase, incompressible
Turbulence model	$k-\omega$ SST
Fluid	Water ($\rho = 998.2\,\mathrm{kg/m^3}$, $\nu = 10^{-6}\,\mathrm{m^2/s}$)
Mesh size	121 000 cells
Time step	Equivalent to 1° rotor revolution
Calculation time	Approx. 70 CPUh on 4 cores

1. Automated mesh generation

A third order B-spline[50] based on the ten node points is used to generate a smooth hydrofoil shape, providing a list of 2000 points for shape definition. The *blockMesh* utility from *OpenFOAM* has been chosen for the mesh generation because it serves perfectly for an automated but fully controlled meshing process. This allows the creation of a high-quality two-dimensional multi-blocks structured mesh and makes the mesh settings comparable in between very different shapes.

With the aim of achieving the exact same mesh structure for all cases, the mesh has been divided into several domains, which are later joined to a final mesh. Figure 4 (top) shows the sub-domains highlighted by different colors. The blue sub-domains are kept exactly the same for all cases, while the green part is meshed individually. The full computational domain and block structure can be seen at the top of the illustration. The bottom of Fig. 4 shows the mesh of the rotor region and gives a closer view of the leading and trailing edges of a blade. The presented mesh corresponds to the reference case.

The mesh defining the blade shape is constructed on the base of an individual *blockMesh* dictionary file for each case, containing the 2000 blade points from the B-Spline interpolation. All sections are merged after meshing the blade sub-domain. To ensure a fully resolved boundary layer at the blade, it has been taken care to satisfy the $y^+ \sim 1$ condition formulated by Maître *et al.* for the use of the k–ω–SST (Shear Stress Transport) turbulence model.[49] Each mesh is validated by the *OpenFOAM* function *checkMesh* prior to the simulations. Table V lists the allowed values of the main mesh quality metrics. This verifies the necessary quality and ensures that the automatically generated meshes conform to best practices.

2. Data generation–numerical simulations

After the mesh has been successfully generated and checked, the 2D CFD simulation is performed. The *pimpleFoam* solver and Menter's $k-\omega-$ SST (Shear Stress Transport) turbulence model[51] are employed to solve the incompressible Unsteady Reynolds-averaged Navier–Stokes (URANS) equations. The governing equations are shown in Appendix A. This turbulence model is known to precisely predict near-wall flows, while ensuring numerical stability and keeping computational costs low. It is widely used in numerical CFTT studies.[4,10,15,19,22,49,52–54]

It should be noted that the applied 2D simulations cannot capture three-dimensional effects such as tip vortices and spanwise flow. In addition, URANS simulations provide a phase-averaged representation of dynamic stall. Therefore, highly transient flow phenomena can only partly be resolved with this approach. Nevertheless, 2D URANS has been widely employed for CFTT studies, as it reproduces force trends with reduced computational costs compared to 3D simulations. This makes the applied method sufficiently accurate and cost-efficient for the relative comparison of blade shapes at the early design stage, which is the main objective of this study.

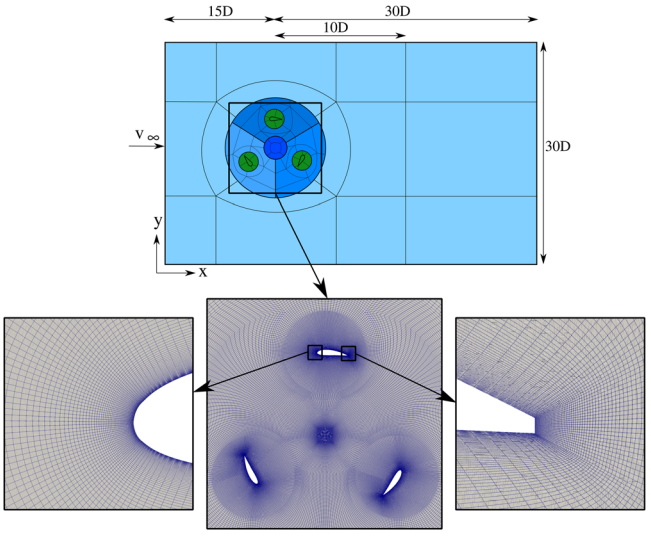

FIG. 4. Computational domain and mesh. Top: Domain and block structure of the mesh. The blue blocks remain constant for each individual, the green blocks represent the individually generated meshes. Note that the image is not to scale. Bottom: Exemplary mesh of the reference case (projected NACA0018 blade with $c = 72.44$ mm) around the rotor region with a close view at the leading and trailing edges.

At the inlet, the velocity was set to $V_\infty = 0.8\,\mathrm{m/s}$ for all simulations, and the turbulence intensity was set to 15% ($k = 0.024\,\mathrm{m^2/s^2}$). However, it dissipates to 0.27% at 1D in front of the turbine ($x = -1D$, $k = 7 \times 10^{-6}\,\mathrm{m^2/s^2}$). Both the inlet velocity and the turbulence in the vicinity of the turbine are comparable to those of the laboratory flume in which the future turbine model will be tested. The outlet pressure was set to 0 Pa. The side walls were set as symmetry boundaries (slip condition), and all blades were set as solid walls with no-slip. The properties of the fluid are listed in Table IV, which in the present case corresponds to water.

To handle the rotation of the turbine, a so-called "arbitrary mesh interface" (AMI) is employed between the interfaces of the different parts of the mesh. This allows the mapping of the flow quantities from one mesh sub-domain onto the adjacent domain. In the present case, the dark blue inner circle and the light blue outer domain (see Fig. 4) are stationary, while the rotation is applied to the annulus and the blade sub-domains. For the rotating motion, the corresponding angular velocity ω_T to the desired TSR is applied to these domains.

TABLE V. Threshold values for the main mesh quality metrics.

Metric	Criterion (accepted)
Non-orthogonality	$<80°$
Skewness	<4
Aspect ratio	<1000

The chord-based Reynolds number covers a wide range from Re = 24 000 to 287 500, due to the different chord lengths (60–90 mm) and TSR (1.5–3.0), as well as the alternating relative speed $\vec{W} = \vec{V}_\infty + \vec{\omega}_T R$ (retrieved from velocity triangles). Even though the Reynolds numbers indicate a transitional flow, it has been chosen to model the flow using the $k-\omega-$SST turbulence model, due to its numerical stability and low computational costs.

With the aim to save computational time and considering the similarity of all cases, all simulations are initialized by mapping the flow field from the reference simulation as an initial condition, which has been run for 40 consecutive revolutions to ensure its full convergence. Tests with a few cases showed a faster convergence and a reduction in calculation time by roughly 20%.

For each case, ten turbine revolutions were simulated with a time step equivalent to 1° rotor revolution. Simulations have been carried out in parallel on four cores. A speed-up study showed that four cores offered the best trade-off between computational efficiency and resource allocation, allowing the execution of 32 different cases simultaneously on the available cluster nodes. The computational time depends on the settings (blade shape and TSR) of each individual. However, the reference case required roughly 14 h, corresponding to 56 central processing unit (CPU) hours to calculate ten turbine revolutions.

C. Evaluation methods

The hydrodynamic forces acting on the blades of a CFTT alternate continuously due to the variation of the angle of attack throughout each revolution. These forces are split up into a tangential component (F_t), responsible for generating torque, and a normal component (F_n), which induces structural loads.[55] The assessment and comparison of different turbine blade designs will be based on these force components, analyzed on the basis of two criteria:

- the performance of the turbine based on F_t by using the power coefficient C_P
- the fatigue failure risk resulting from F_n determined by the stresses, which were condensed into a single dimensionless coefficient C_σ

All CFD simulation results were processed employing the *FluidFoam package*[56] in Python.

1. Performance prediction

As aforementioned, the performance assessment is based on the dimensionless power coefficient C_P, which allows for the comparison of different turbine rotor sizes and designs. Equation (2) shows its definition, where Q is the turbine torque, ω_T the angular velocity, ρ the water density, A is the projected cross section of the runner, and V_∞ the undisturbed inflow velocity:

$$C_P = \frac{P_{\text{mech}}}{P_{\text{flow}}} = \frac{Q \cdot \omega_T}{0.5 \cdot \rho \cdot A \cdot V_\infty^3}. \tag{2}$$

2. Blade loading

The 2D CFD simulations provide the chord-wise pressure distribution for each time step. To assess the stresses in the structure, a 3D mechanical model is necessary. With the aim of providing a simple analytical model with reduced complexity, the blades have been modeled as a beam structure clamped on both ends. The pressure loads and the viscous shear forces lead to the normal force F_n on the blade. In our model, this normal force is extruded over the span of the blade (in z-direction) and is therefore accounted for by an evenly distributed line load q, that acts over the entire length of the blade. It is assumed that the flow behaves uniformly along the water column (z-axis). This assumption is necessary because the conducted 2D CFD simulations will not provide the real non-uniform spanwise pressure distributions.

The tangential force F_t is not accounted for in the fatigue risk assessment, as it is considered to be less critical for the structural health but driving the turbine. Following these assumptions and simplifications, the EBB theory for uniformly distributed single-axis loads can be applied.

The forces and moments acting on both clamped ends, the supports A and B, are calculated following the method proposed by Luévanos Rojas and Montoya Ramírez[57] using the Euler–Bernoulli beam theory with Eqs. (3) and (4), where L is the blade length, equal to 400 mm in this study. The governing equations and boundary conditions used are provided in Appendix B.

$$F_{\text{AB,y}} = \frac{q \cdot L}{2}, \tag{3}$$

$$M_{\text{AB}} = \frac{q \cdot L^2}{12}. \tag{4}$$

The internal shear forces F_q in the y-direction and bending moments M_b around the x-axis will lead to shear τ and bending σ_b stresses. They are determined following Eqs. (5) and (6), with z being the location of the blade, where the force and moment shall be calculated:

$$F_q = q \cdot \left(\frac{L}{2} - z\right), \tag{5}$$

$$M_b = \frac{q}{2} \cdot \left(L \cdot z - z^2 - \frac{L^2}{6}\right). \tag{6}$$

The peak magnitudes of both, F_q and M_b, are highest at the clamped ends of the blade ($z = 0$ mm and $z = 400$ mm), which corresponds to the location of the blade-strut connection on the turbine. With respect to the uniform pressure distribution and rotor symmetry, only one point ($z = 0$ mm) will be assessed. Shear τ and bending stresses σ_b are calculated with Eqs. (7) and (8) respectively, where S is the cross section of the blade, and Z is the section modulus:

$$\tau = \frac{F_q}{S}, \tag{7}$$

$$\sigma_b = \frac{M_b}{Z}. \tag{8}$$

Given the structural design of the turbine prototype, a combination of 3D printed polymer parts and shells together with an aluminum skeleton, it is reasonable to focus on the metallic structure. In this case, a 12 mm stainless steel rod builds the connection between the blades and the struts, which has to withstand and transfer the loads from the blades to the support. This point can be considered to be the most critical. Weak coupled fluid-structure interaction simulations, employing CFD (*OpenFOAM*) and FEA (*Ansys Mechanical*) on the flume model support this consideration.[21,58] Therefore, both the cross

section S and the section modulus Z of the blade are calculated in relation to the rod, the material properties of which can be found in Table I. Thus, the occurring stresses are accordingly evaluated at the blade-strut junction, located at the tips of the blades ($z = 0$ mm and $z = 400$ mm).

The beam undergoes both shear and bending stresses. As the beam length is significantly larger than the beam thickness, the shear stresses τ are generally considerably smaller than the bending stresses σ_b. In consequence τ has been neglected for further assessment following the recommendations from Refs. 59 and 60.

The dynamically alternating loads repeat periodically for each turbine revolution. Therefore, the bending stress is calculated for each time step of the last revolution, resulting in 360 calculation points. The fatigue limit can be assessed with the use of the Smith diagram, which accounts for static and dynamic effects in the fatigue risk assessment.[40,59,61] Following this method, the magnitude of stress peaks (max $|\sigma_{amplitude}|$) are plotted against mean stress ($|\sigma_{mean}|$) as both dynamic and static loads are important for the fatigue strength of a structure. In this study, a combined stress value $\sigma_{combined}$ is defined, which is based on the aforementioned method. The definition is given in Eq. (9):

$$\sigma_{combined} = \sigma_{amplitude} + \sigma_{mean}. \tag{9}$$

The peaks $\sigma_{amplitude}$ and the mean σ_{mean} stresses of the periodical loads are calculated as stated in Eqs. (10) and (11), where $\sigma_{b,max}$ is the maximal experienced bending stress during the last revolution of the turbine and $\sigma_{b,min}$ the minimal stress:

$$\sigma_{amplitude} = \frac{\sigma_{b,max} - \sigma_{b,min}}{2}, \tag{10}$$

$$\sigma_{mean} = \frac{\sigma_{b,max} + \sigma_{b,min}}{2}. \tag{11}$$

The combined stress $\sigma_{combined}$ is expressed as a dimensionless coefficient by division of $\sigma_{combined}$ by the dynamic pressure p_∞ from the flow velocity at the inlet V_∞, as shown in Eq. (12). The resulting stress coefficient C_σ provides a single dimensionless parameter for the assessment of the relative fatigue risk compared to other profiles and operation points. Therefore, C_σ is a relative indicator suitable for early design stage assessments, and it does not replace a full fatigue-life analysis based on S–N curves. It is a simplified metric that does not for account additional loads, such as torsional and shear stresses on the blade, or forces acting on the turbine structure. Nevertheless, a higher value of C_σ would, for a given material, correlate with a lower number of cycles to failure.

$$C_\sigma = \frac{\sigma_{combined}}{p_\infty} = \frac{\sigma_{amplitude} + \sigma_{mean}}{0.5 \cdot \rho \cdot V_\infty^2}. \tag{12}$$

It is obvious that C_σ should be minimal in order to raise the possible turbine lifetime and to allow for material saving with a load adapted rotor design. To conclude, two parameters are evaluated in order to assess the suitability of a given parameter set (blade profile and TSR) for a high performing rotor design along with good machinery lifetime: C_P, which should be as high as possible as it stands for the turbine performance and C_σ, which is a measure for the fatigue failure risk and thus should be as low as possible. These two dimensionless indicators make it possible to evaluate a large number of parameter sets in a fast, automatized and reliable manner, resulting in several optimal cases, of which the user has to decide on the best trade-off for the application.

III. VERIFICATION AND VALIDATION

A. Mesh and time sensitivity analysis

A grid sensitivity study was carried out on the reference configuration (cambered NACA0018, $c = 72.44$ mm at TSR = 2.25). The study was divided into two parts. This allows for an independent assessment of the sensitivity of the results to the mesh resolution of: (1) the blade disks (in green in Fig. 4) and (2) of the remaining computational domain (in blue in Fig. 4). The converged mesh contains 121 000 cells, with 219 cells around each blade. Further details are provided in Appendix C.

A time step sensitivity study has also been conducted. For this purpose, the reference configuration was simulated using six different time steps corresponding to the variation of the turbine's azimuth angle of 8°, 4°, 2°, 1°, 0.5°, and 0.25°. This was conducted for two different operating points: a TSR of 2.25 and 1.5, the latter being the most challenging TSR that might be faced in the present study due to blade stall occurrence. Following this study, a time step corresponding to the variation of the turbine's azimuth angle of 1° has been chosen, as it results in the best trade-off between the accuracy, having a percentage deviation lower than 1% for a TSR of 2.25, and the computational time, which is much lower than for smaller time steps. See Appendix D for further details.

B. Validation

The employed mesh and the numerical setup previously presented will be validated by numerically recreating the experiments conducted by Clary *et al.*,[53] who conducted measurements of a straight-bladed Darrieus turbine in a water tunnel. The turbine employed in their study is made of three blades and has a diameter of 175 mm. The blades consist of a NACA0018 foil with a chord length of 32 mm, whose mean line was fit to the turbine circumference to create a cambered blade, similar to the blade shape of the reference case in the present study. The 2D geometry of our turbine ($D = 400$ mm) corresponds to a scaled version of the turbine from Clary *et al.* ($D = 175$ mm).

The mesh described in Sec. II B 1 was generated in a parameterized way, allowing for a quick adaptation to the size and blade shape of the turbine studied by Clary *et al.*, ensuring the exact geometry of the turbine and therefore the validity of the mesh. The domain was kept as described in Sec. II B 1 (see Fig. 4) and only the blade geometry and the dimensions of the turbine were adjusted, leading to a mesh with about 121 000 cells.

The exact same numerical set-up described in Sec. II B 2 has been used. URANS computations are performed, and the $k-\omega-$SST turbulence model is employed. Each simulation was conducted for ten turbine revolutions with a time step corresponding to 1° variation of the azimuth angle. The only modifications made to the set-up were case related changes. Here, the inlet velocity has been set to $V_\infty = 2.3$ m/s, corresponding to the experiments from the validation case.[53] Also the turbulence intensity was set to 5.5% ($k = 0.024\ m^2/s^2$) and the turbulence specific dissipation rate ω to 9 1/s. All other boundary conditions were kept equal to the ones in Sec. II B 2. The chord-based Reynolds number ranges from Re = 37 000 to 294 000 for the experimental data and the numerical validation, being in a

comparable range to the numerical setup described in Sec. II B 2 (Re = 24 000–287 500).

Figure 5 shows the characteristic curve obtained from the CFD simulations (shown in black with circle markers), as well as the experimental results by Clary *et al.*[53] (shown in blue with square markers). It can be seen that the C_P value of the numerical simulations is over-predicted for all studied TSR except the ones lower than 1.25. This trend is consistent with similar results found in the literature, such as the ones presented by Maître *et al.*,[49] Li *et al.*[62] or Gosselin *et al.*[63] For TSR values lower than 1.5, the turbine is highly affected by primary effects where the blades experience stall. This phenomenon is known for not being correctly predicted by URANS simulations. For this reason, in the present study, it has been chosen to restrict the operating points between TSR of 1.5 and 3.0, to avoid the deep stall regime. For TSR values above 2.25, the numerical C_P value has a linear offset from the experimental value. This offset is caused by secondary effects, such as tip vortices and blade/arm junction losses, which are not modeled in the 2D simulations.[49,62–65] In the observed region between TSR = 1.5 and 3.0 an absolute difference between the experimental and 2D numerical results of 0.1 in the C_P is found, which corresponds to a relative difference of 56.9%. This is a known effect, found, for example, by Maître *et al.*, where the experiments featured a $C_P = 0.34$ and the 2D CFD a $C_P = 0.58$.[49] In addition to this difference, it can be seen that the optimal TSR is well reproduced with the simulation, as both curves find their peaks at about TSR = 1.75. This accurate representation of the curve trend and the peak position are of great relevance in the context of the present work. In consequence, the simulation setup can be considered to be adequate for the qualitative comparison of the performance (C_P) of multiple blade shapes as it is intended in the study at hand.

IV. RESULTS AND DISCUSSION

A. Distribution of the blade shapes

In total, 120 hydrofoil shapes have been generated and assessed, each of these with a set of different operating points, chord lengths and shapes. The differences in the latter, can best be illustrated through the broad range of blade mean thickness and their maximal camber. The distribution of the different blade shapes can be seen in Fig. 6, where the color of the points describes the assigned TSR and the size of the points the maximal camber of the shape. Four profile shapes have been arbitrary selected in addition to the reference for a spot analysis to examine their performance in detail. The parameter of the selected cases are listed in Table VI.

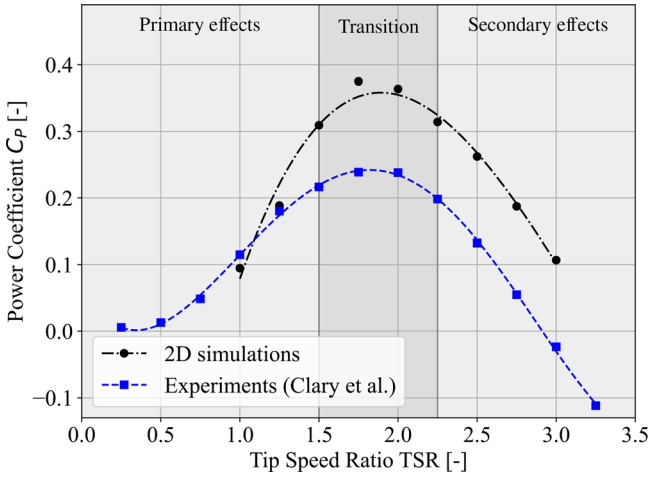

FIG. 5. Power coefficient C_P as a function of the TSR. Comparison between the experimental results from Clary *et al.*[53] and the numerical simulations (URANS, $k-\omega-$SST turbulence model). A 4th-degree polynomial trend line has been used to connect the data points for clarity.

Figure 7 shows the distribution of the different variables to visualize the effectiveness of the pseudo-randomized Sobol initialization. It can be seen that the design space of the TSR as well as the chord length are almost equally covered. However, the distribution of mean thickness, maximal camber as well as tortuosity show a non-uniform distribution. This is due to the parameter constraints. The maximal thickness is imposed at the quarter chord location with 13 mm and the blade is forced to get thinner at the leading and trailing edges. Also, only cambering the blade in the downwards direction with a maximal y-location of the points is imposed. The same applies for the tortuosity, where a high tortuosity describes blades with a very snake-like bending along the camber line, which is very difficult to generate due to the given constraints and also not considered to be meaningful by the authors.

The different hydrofoil shapes have been evaluated following the methods presented in Sec. II C and the results are shown in Fig. 8, which shows a scatterplot of the power coefficient C_P on the x-axis and the stress coefficient C_σ on the y-axis. It can be seen that the utmost of the cases range from $C_P = -0.5$ to $C_P = 0.36$ and $C_\sigma = 0.26 \cdot 10^5$ to $C_\sigma = 0.8 \cdot 10^5$, with some outliers showing even lower C_P and higher C_σ values. Cases with a negative power coefficient are generally uninteresting, as they do not generate power, and therefore, no longer represent a turbine. For this reason only cases with a positive C_P value have been included as possible spot analysis candidates.

In general, no clear trend between the power and the stress coefficient can be found in Fig. 8. However, the highlighted cases A, B and the reference case can be considered as the most favorable cases, as they deliver a high C_P with low C_σ. For these cases a tendency can be seen in the zoomed in section on the right of the plot, where an increase in the power coefficient is accompanied by a higher stress coefficient. However there are also few cases that have both a very high C_σ paired with a low C_P. These cases feature an undesired design and reflect the importance of a meaningful blade shape.

Figure 9 presents a parallel coordinate plot that visualizes the relation between the design parameters of each blade shape and their corresponding evaluation result. The wide spread of lines across each axis reflects the broad spectrum of tested hydrofoil shapes, giving insight into the design space covered in the present study. The five selected cases have been highlighted with different colors and line styles to better track their values. It can be seen that the cases C and D have high chord lengths and lower tip speed ratios, which seems to lead to a lower C_P and higher C_σ. It has to be noted that the lower C_P could be caused by the fact that a lower TSR usually results in higher angles of attack on the blade, leading to flow separation (stall) and therefore a decreased power output. At the same time the higher chord lengths lead to increased hydrodynamic forces, which may therefore cause the higher C_σ values.

In order to further analyze the correlation between the different design variables and the results, the variables have been displayed in

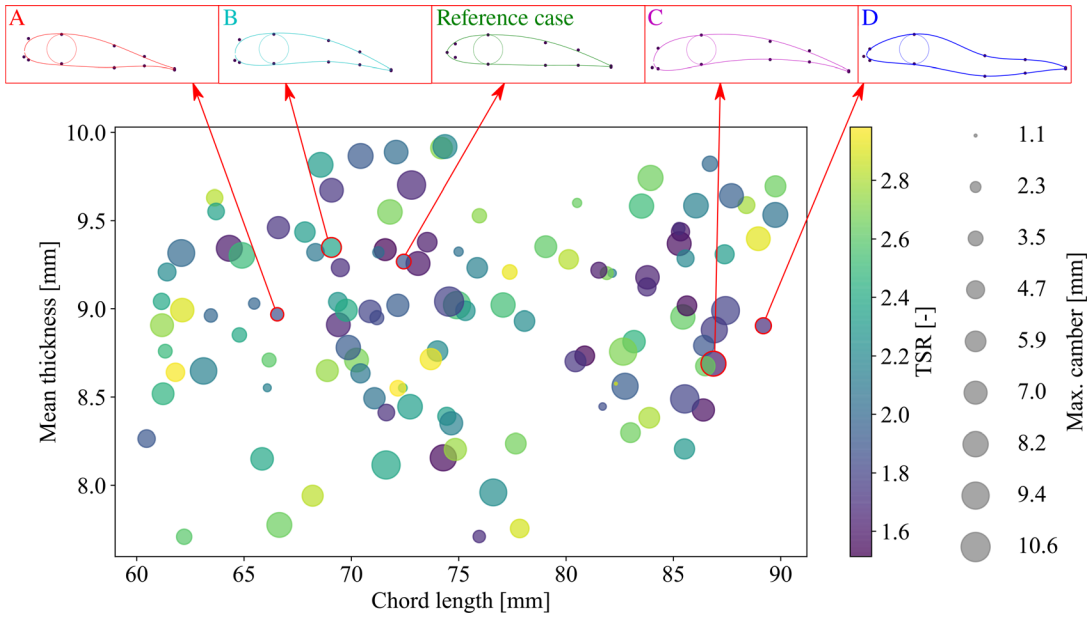

FIG. 6. Distribution of the 120 assessed blade shapes and arbitrarily picked four design cases for further spot analysis.

TABLE VI. Values of the design space variables of the five picked cases.

Variable	Ref. case	Case A	Case B	Case C	Case D
Tip speed ratio (-)	1.9	1.9	2.4	1.6	1.7
Chord length (mm)	72.4	66.6	69.1	86.9	89.2
Mean thickness (mm)	9.3	9.0	9.4	8.7	8.9
Maximal camber (mm)	3.5	2.9	5.5	8.1	3.9
Tortuosity (-)	1.01	1.01	1.02	1.03	1.01

scatter plots against C_P in Fig. 10 and C_σ in Fig. 11. In addition, the Pearson correlation value has been calculated and is displayed in a table in the bottom right of the figures.

When looking into the correlation between the variables and the power coefficient it can be noted that a strong negative correlation below −0.6 exists between C_P and the maximal camber as well as the tortuosity. For these two parameters, an additional regression line has been added to the plot. Both variables describe a similar characteristic of the blade shapes, namely their bending. Their negative correlation values indicate an inverse relation, meaning that a low value for the maximal camber and the tortuosity leads to higher power coefficients. This implies that a blade design with a small camber performs better,

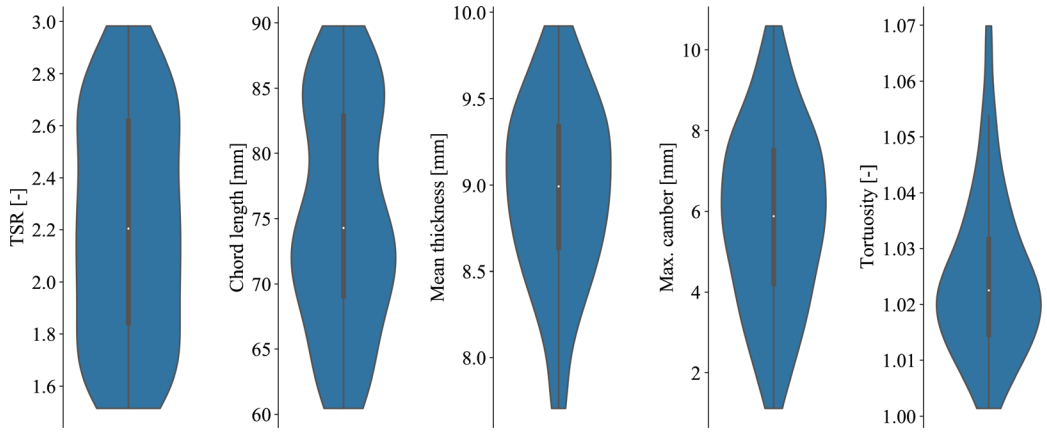

FIG. 7. Violin plot showing the distribution of chord length, mean thickness, maximum camber, tortuosity, and TSR for the 120 automatically generated cases analyzed in the present study.

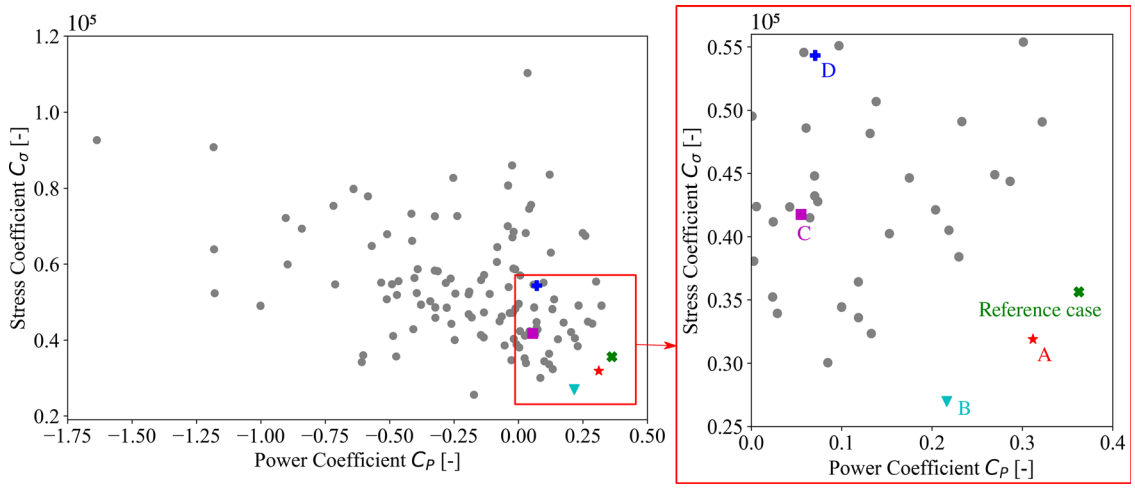

FIG. 8. Result of the evaluation of the different blade shapes with respect to the stress coefficient C_σ and the power coefficient C_P.

which underlines classical blade design practices. At the same time, the cambering of the blade does not appear to influence the stress coefficient C_σ, as no correlation can be observed in the set of considered cases shown in Fig. 11. This effect could be an advantage for morphing blades. However, existing studies do not provide a clear picture in this regard. While Hoerner *et al.* found a reduction of loads for chordwise flexible blades, Liu *et al.* reached the opposite conclusion.[5,66] Therefore, further studies are necessary on this topic.

The spot analysis of the selected cases in Fig. 9 suggests a correlation between the chord length and the TSR with the power coefficient. This combined effect of c and TSR on the turbine performance has been described in the literature, such as Shiono *et al.*[48] It has been found that larger chord lengths increase torque, but also shift the optimal operating point toward lower TSR. Consequently, the stall effects are more pronounced, reducing the turbine power. However, this effect can not be confirmed by the presented dataset, as the single value correlations can not account for the coupled effect of multiple parameters on an objective. Therefore, no measurable correlation can be found between c, TSR, and C_P. Nevertheless, when looking into the correlation of these variables with the stress coefficient, a quite weak but measurable correlation above 0.3 between C_σ and the chord length and the TSR can be found. In this case, larger chord lengths and TSR lead to increased stress on the blades. This confirms the knowledge from the literature that larger blade shapes increase the hydrodynamic loads on the blades due to higher blade-to-blade interaction.

It would be useful to increase the sample size of the data set in order to further investigate these expected correlations with a better coverage of the entire design space and higher statistical significance. This

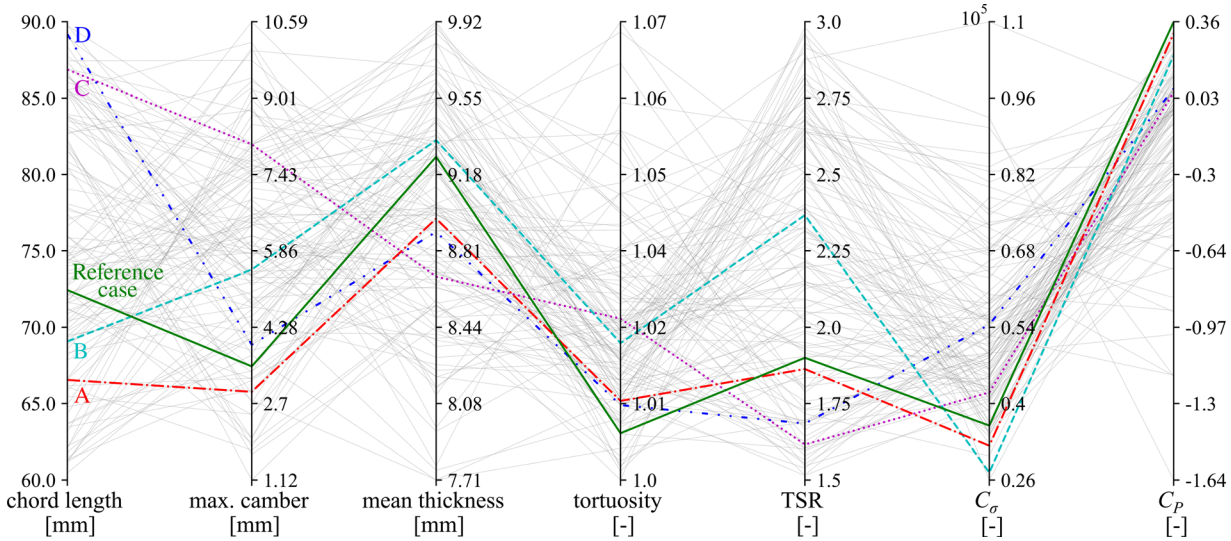

FIG. 9. Parallel coordinate plot showing the characteristic variables of each blade and the result for the stress coefficient C_σ and the power coefficient C_P.

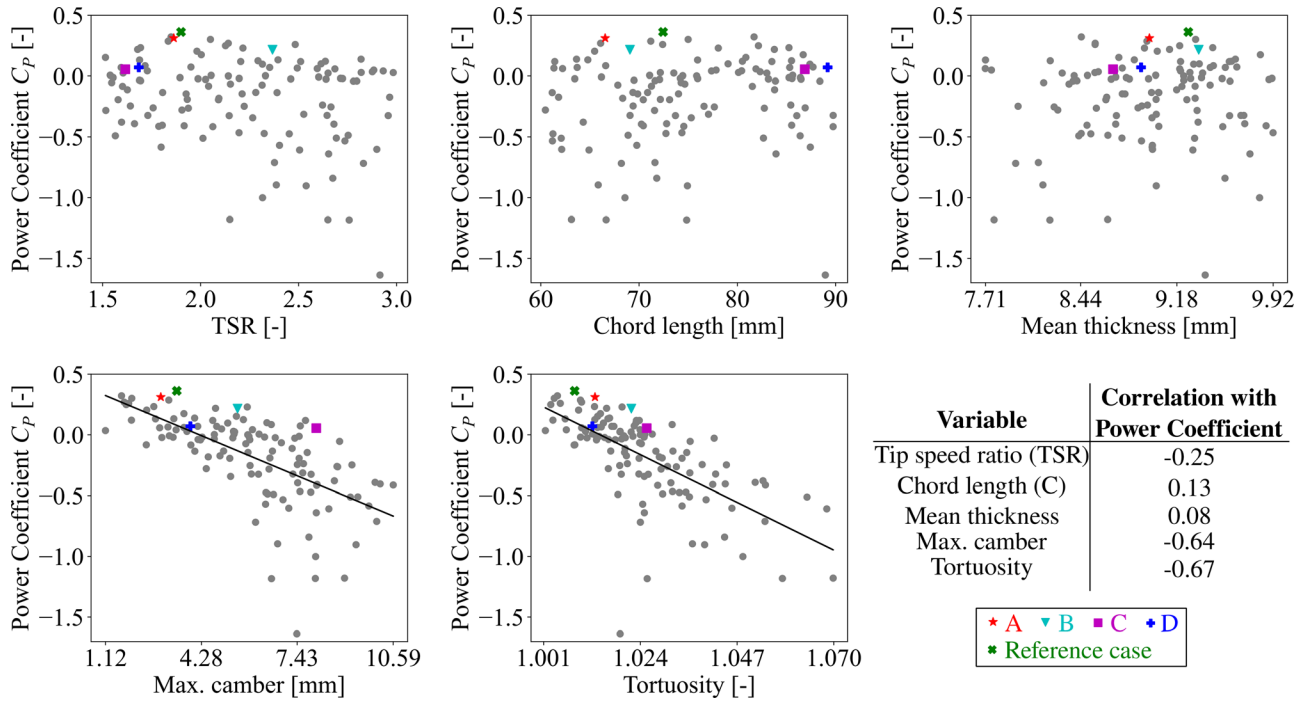

FIG. 10. Matrix of scatter plots showing the distribution of the variables with the power coefficient C_P. The Pearson correlation coefficients for each plot is added in the bottom right table. Because of the higher correlation for maximal camber and tortuosity (bottom left and center plot) a regression line has been added to visualize the parameter correlations.

would enable other statistical methods to be applied in order to study the interdependent effects of the variables, thereby helping to confirm known effects from the literature, as well as revealing unknown correlations. However, the data set does not show a quantifiable effect on C_σ by the bending of the blade or the maximal camber and the tortuosity.

B. Random sample check

From the illustrations of the selected blade shapes in Fig. 6, it can be seen that most of the shapes have a classical cambered blade shape, while case D is similar to the auto-morphed blade shape obtained by an oscillating flexible blade such as presented by Liu *et al.*[67] Case A and the reference case have a lower cambering and a similar operating point, while featuring the highest power coefficient of the selected cases. It is hypothesized that their current operating point is close to the optimal TSR for the presented condition, leading to such a high power output. In comparison, case C features a stronger bending compared to the other cases, which is reflected in the high values for the tortuosity and maximal camber. This case also features a high value for C_σ, underlining the correlation shown in Fig. 11. However, this high C_σ might also be given by the large chord length that causes higher hydrodynamic loads. To further understand the effects of each case on the turbine loadings and power, their instantaneous force coefficients and flow fields are shown in Figs. 12 and 13.

Figure 12 presents the instantaneous tangential and normal force coefficients C_t and C_n as a function of the azimuth angle for the last simulated revolution of the selected cases. The force coefficients have been normalized by dividing the respective force on one blade by a reference force F_{flow}. The latter has been calculated using the turbine's projected cross section area A and the inflow velocity V_∞, as stated in Eqs. (13) and (14). The tangential force coefficient is an indicator for the energy extraction, while the normal force coefficient gives insight into the structural loads on the blade.

$$C_t = \frac{F_t}{F_{flow}} = \frac{F_t}{0.5 \cdot \rho \cdot A \cdot V_\infty^2}, \tag{13}$$

$$C_n = \frac{F_n}{F_{flow}} = \frac{F_n}{0.5 \cdot \rho \cdot A \cdot V_\infty^2}. \tag{14}$$

In addition to the force coefficients, the vorticity fields of the five cases have been displayed for three selected azimuth angles ($\theta = 100°, 170°, 240°$) in Fig. 13. These angles have also been marked with a vertical dashed line in Fig. 12. In Fig. 13, water flows from left to right.

The analysis of the curves of C_t in the left plot in Fig. 12 shows that cases A, B, and the reference case have a similar curve trend. These three cases have their maximal amplitudes at an azimuth angle θ of about 100°, which is then followed by a drop at $\theta = 170°$ and a second lower maxima around $\theta = 200°$. High tangential forces indicate that the blade generates a high driving torque on the turbine shaft. This is the case between the azimuth angles of $\theta = 40°$ and $\theta = 160°$. A similar C_t curve trend is found in the literature for Darrieus turbines spinning at their optimal operating point, such as shown by Sansone *et al.*[68] and Alqurashi and Mohamed.[69]

The main difference between the three cases is that C_t for case B is overall lower than for case A and the reference. This is also reflected

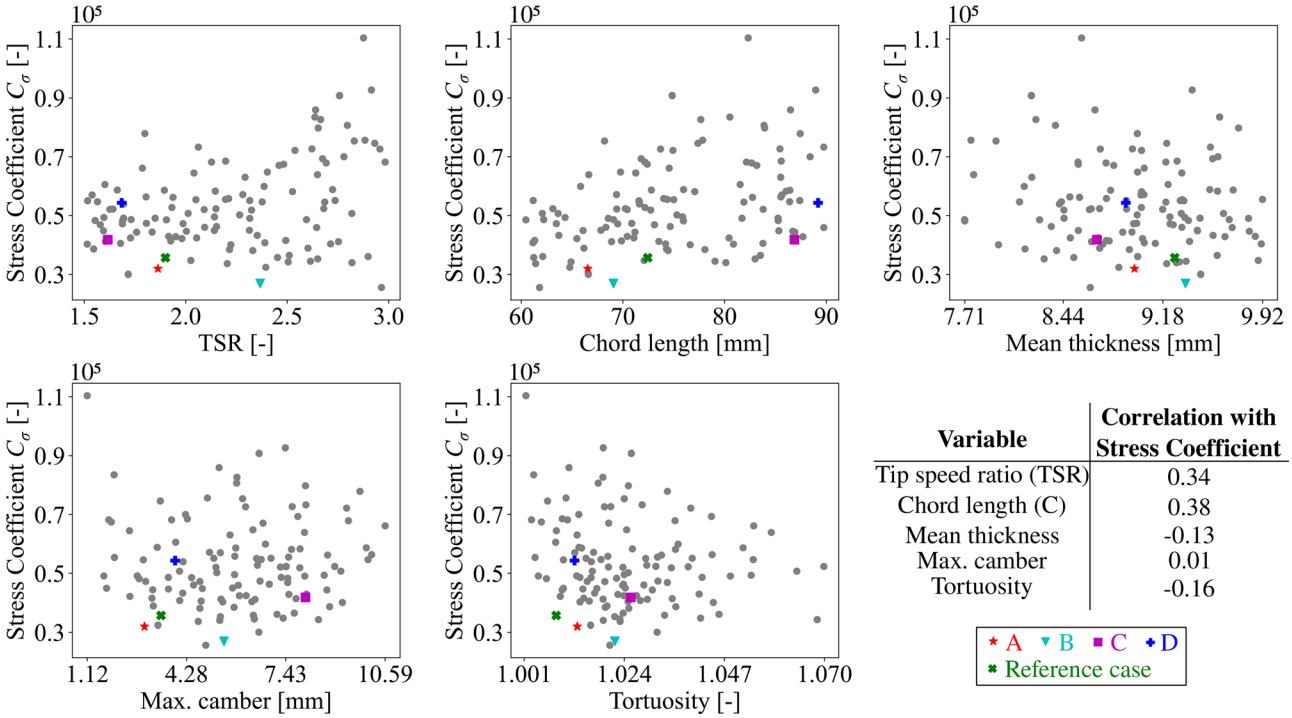

Variable	Correlation with Stress Coefficient
Tip speed ratio (TSR)	0.34
Chord length (C)	0.38
Mean thickness	-0.13
Max. camber	0.01
Tortuosity	-0.16

FIG. 11. Matrix of scatter plots showing the distribution of the variables with the stress coefficient C_σ. The Pearson correlation coefficients for each plot is added in the bottom right table.

by the average C_P of the cases. The lower C_t value for case B could be caused by the cambering of the blade. Out of these three cases, case B features a high camber, which causes negative angles of attack, and thus, reduces torque. This also explains the correlation between the blade camber and the power coefficient shown in Fig. 10. Another difference between the cases is that after passing an azimuth angle of 240°, the curve of case A features fluctuations, while the curves of case B and the reference case remain rather smooth. This might indicate that for case A, the critical angle of attack is exceeded at $\theta = 140°$, causing the blade to stall. When looking at the vorticity fields in Fig. 13, it can be seen that at $\theta = 240°$ the flow on blade one is very similar for cases A, B, and the reference. However, for $\theta = 170°$ it can be seen that blade 3 of case A (positioned at $\theta = 290°$) has shed vortices. This confirms the observation that for case A blade stalls between $\theta = 240°$ and $\theta = 300°$, showing that this blade geometry is more sensitive to stall than case B and the reference case.

For cases C and D the curve trend is different from that for the other cases. Their force amplitude is already reached at about $\theta = 80°$, followed by a sharp force drop with its minimum at $\theta = 100°$. Several smaller force peaks follow until about $\theta = 240°$ when the curve

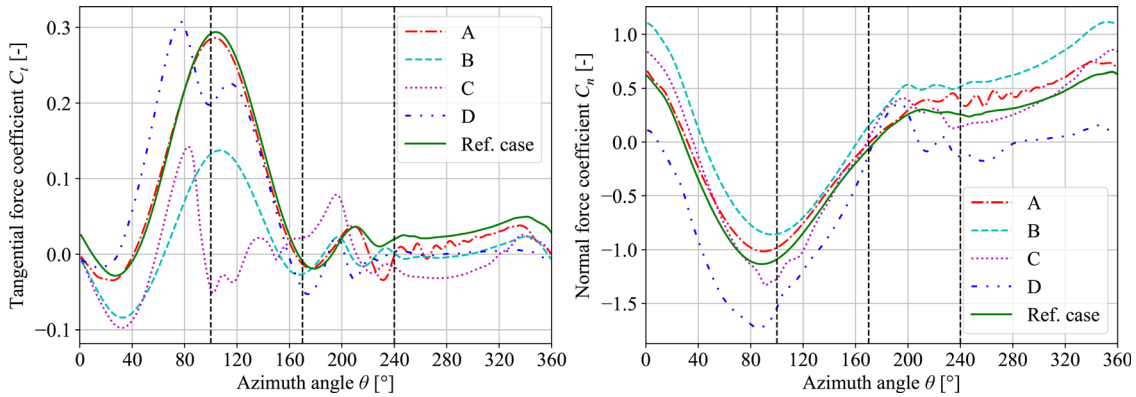

FIG. 12. Instantaneous tangential and normal force coefficients C_t and C_n for one blade of the selected cases during the tenth simulated revolution. The reference force has been calculated with the turbine cross section.

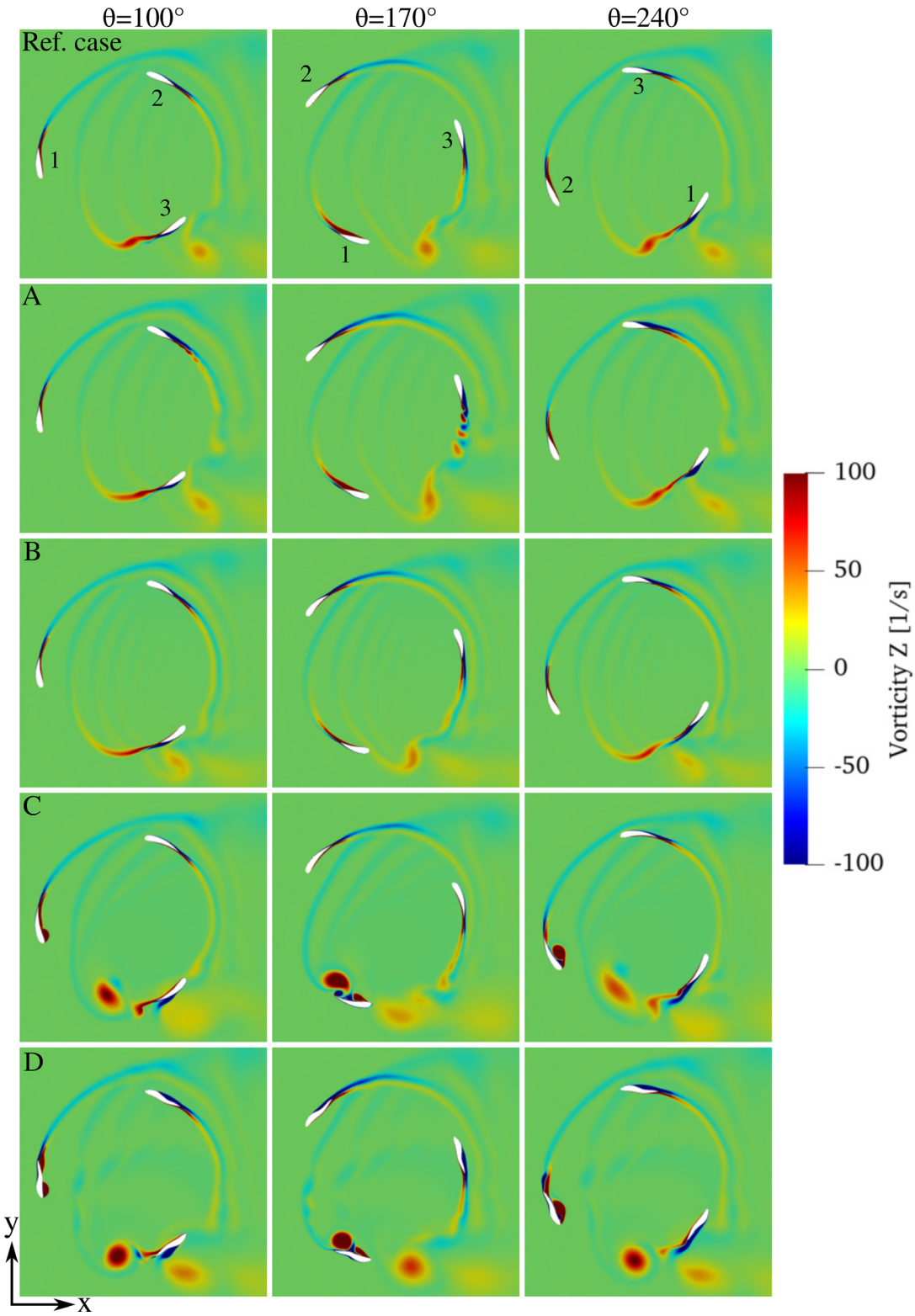

FIG. 13. Vorticity fields of the selected cases for the azimuth angles $\theta = 100^\circ, 170^\circ, 240^\circ$ for blade 1. Water flows from left to right.

TABLE VII. Amplitude and mean bending stress value for the tenth turbine revolution of selected cases.

Case	$\sigma_{amplitude}$ (MPa)	σ_{mean} (MPa)	C_σ (-)
A	8.85	1.34	0.32
B	9.9	−1.29	0.27
C	10.97	2.37	0.42
D	10.48	6.87	0.54
Ref. case	8.96	2.42	0.36

stabilizes. This curve trend typically indicates blade stall: flow detaches massively from the blade causing this sudden drop of the tangential force. In Fig. 13 it can clearly be seen that the flow detaches at $\theta = 100°$ on the suction side of the leading edge of blade one. At $\theta = 170°$ a large vortex structure is shed from the trailing edge showing the blade stall. These characteristics are only found for cases C and D. Both cases feature high chord lengths but in particular, low TSR which is known from velocity triangles to cause the blade to pass the stall angle and cause the flow detachment.

To summarize the vorticity fields, cases A, B, and the reference case show a smoother course when compared to cases C and D. In these latter cases, stalling occurs at about $\theta = 100°$. A significant vortex is built up on the suction side of the blade. However, case A still features a small vortex shedding between $\theta = 240°$ and $\theta = 300°$. This is also reflected in the curve trend of C_t.

Looking at the normal force coefficient curves, all five cases show a similar trend. The curves find their minimum C_n at about $\theta = 100°$, which is approximately the azimuth angle leading to the maximum angle of attack of the blade. This causes an important negative normal force on the blade (directed inwards), which would cause a high bending of the blade. After this, the magnitude of C_n decreases until reaching the zero point at $\theta = 160°$, where the force changes from tensile to compressive force. Up to about $\theta = 200°$ the C_n value increases rapidly, followed by a very slow increase until the end of the rotation. The main difference between the five cases is not found in the general curve slope over a rotation but in their magnitudes, which leads to differences in the averaged stress coefficient C_σ.

Table VII lists the amplitude and the averaged bending stress for the tenth turbine revolution for the selected cases, as well as the resulting stress coefficient C_σ. As expected from the C_n plot, the amplitude of the bending stress takes a quite similar value between 8.8 and 11 MPa for all five cases. However, at the same time, the mean values are much lower in general, but have a high variation in between −1.2 and 6.9 MPa. This underlines the necessity to account for the mean load in the structural analysis and to use the approach based on the Smith diagram as proposed in the presented method. It can be seen that Case D has both one of the highest $\sigma_{amplitude}$ and the highest σ_{mean} value. This is also reflected in the C_σ value, which is the highest for the five cases. Otherwise, case A features the lowest $\sigma_{amplitude}$ as well as a quite low mean bending stress, which is also illustrated in its low C_σ value. It can be concluded that the presented methodology is suitable for assessing the complex instantaneous blade loads with a single value.

V. CONCLUSION

In the present paper, a standardized, systematic, and automated methodology to assess the loads on the structure of a cross-flow tidal turbine in a cost efficient and accurate manner has been presented. The methodology is based on fully automated CFD simulations, which allow for evaluation of the performance and structural loads. The latter are based on a simplified mechanical model of the blade represented as a clamped beam, and the assessment of the most critical point at the fixation. A stress coefficient is introduced that accounts for both amplitude and mean stress of the alternating loads, providing a simple yet accurate way to qualitatively compare the fatigue risk in different designs of cross-flow tidal turbine blade shapes and operating points. It should be noted that C_σ is a relative indicator of fatigue risk. It is suitable for comparing different blade profiles and operating conditions at an early design stage, but it does not replace a full fatigue life prediction for the entire turbine.

To assess the methodology, 120 cases with randomized blade shapes and different operating points have been analyzed. The diameter of the turbine is limited by the experimental setup, and therefore, fixed at 400 mm for all cases. However, the tested blades had different shapes and chord lengths (60–90 mm), which allowed to test a wide range of solidities ($\sigma = 0.9$–1.35). The analysis of the different cases revealed preliminary correlations in between the design parameters and the turbine power and stress coefficients. The analysis showed that blade cambering, quantified by maximal camber and blade tortuosity, has a high correlation with the blade performance. It shows that more pronounced cambering leads to lower C_P. However, it does not indicate a significant effect on the blade loads. This could suggest that morphing blades could be a feasible concept to adapt the turbine performance without increasing loadings. However, further research is necessary on this topic, as existing studies do not provide a clear picture. In addition, a weak correlation was found for larger chord lengths and higher tip speed ratios, which increase the stress coefficient. In comparison, no meaningful correlation between these parameters and the C_P was found. Nevertheless, the in-depth spot analysis of five different cases suggests that the TSR and c have an impact on the C_P value, which is also known from literature. Therefore, the effect of TSR and c on both C_σ and C_P should be investigated with higher sample sizes to provide better statistical relevance.

In summary, the proposed method enables a fast, accurate, and systematic assessment of CFFT structural loads without the need for computationally expensive FSI simulations. In addition, the setup is suitable for fully automatized assessment of different cases, avoiding the coupling of two heavy software solutions for the CFD and FEA while providing the important information by only two dimensionless indicators (C_P and C_σ). An optimal case can then be selected from the Pareto front as a trade-off between C_P and C_σ, depending on the specific requirements. This makes it particularly useful for early-stage design optimization as well as a comparative metric of turbine blades and operating points. The study also clearly emphasizes the importance of optimized turbine geometries for balancing the power output with the structural lifetime of cross-flow tidal turbines.

ACKNOWLEDGMENTS

This work was funded by the Deutsche Forschungsgemeinschaft [DFG (FKZ: 457325924)] and the labex Tec21 Investissements d'avenir—agreement n°ANR-11-LABX-0030. Part of the computations presented in this paper were also performed using the GRICAD infrastructure. We are grateful to the developers involved in OpenFOAM software.

AUTHOR DECLARATIONS

Conflict of Interest

The authors have no conflicts to disclose.

Author Contributions

K. Ruiz-Hussmann: Conceptualization (equal); Data curation (lead); Formal analysis (equal); Investigation (equal); Methodology (equal); Software (equal); Writing – original draft (lead). **P.-L. Delafin:** Conceptualization (equal); Formal analysis (equal); Funding acquisition (equal); Methodology (equal); Project administration (equal); Resources (equal); Software (equal); Supervision (equal); Writing – review & editing (equal). **T. Bennecke:** Investigation (equal); Methodology (equal); Software (equal); Writing – review & editing (equal). **C. Bonamy:** Conceptualization (equal); Formal analysis (equal); Methodology (equal); Resources (equal); Software (equal); Supervision (equal); Writing – review & editing (equal). **S. Hoerner:** Conceptualization (equal); Formal analysis (equal); Funding acquisition (equal); Methodology (equal); Project administration (equal); Resources (equal); Software (equal); Supervision (equal); Writing – review & editing (equal).

DATA AVAILABILITY

The data that support the findings of this study are available from the corresponding author upon reasonable request.

NOMENCLATURE

A	Projected cross-section area of the turbine (m^2)
C_n	Normal force coefficient (-)
C_P	Power coefficient (-)
C_Q	Torque coefficient (-)
C_t	Tangential force coefficient (-)
C_σ	Stress coefficient (-)
CAD	Computer-aided design
CFD	Computational fluid dynamics
CFTT	Cross-flow tidal turbines
CPU	Central processing unit
c	Blade chord length (m)
D	Turbine diameter (m)
DNS	Direct numerical simulation
E	Young's modulus (GPa)
EBB	Euler–Bernoulli beam theory
$F_{AB,y}$	Force on the supports A and B in y-direction (N)
F_{flow}	Reference force of the incoming flow (N)
F_n	Normal force (N)
F_q	Shear force (N)
F_t	Tangential force (N)
FEA	Finite element analysis
FSI	Fluid–structure interaction
HAT	Horizontal-axis turbines
k	Turbulent kinetic energy (m^2/s^2)
L	Length of the turbine blade (m)
LEGI	Laboratoire des Ecoulements Geophysiques et Industriels
l	Length of the blade camber line (m)
M_{AB}	Moment on the supports A and B (Nm)
M_b	Bending moment (Nm)
NACA	National Advisory Committee for Aeronautics
p_∞	Dynamic pressure of the flow (Pa)
Q	Turbine torque (Nm)
q	Distributed line load (N/m)
R	Turbine radius (m)
R_m	Tensile strength (MPa)
R_p	Yield strength (MPa)
Re	Reynolds number (-)
S	Cross-section of the blade (m^2)
SST	Shear stress transport
T	Temperature (°C)
TSR	Tip speed ratio
URANS	Unsteady Reynolds-averaged Navier–Stokes
V_∞	Absolute flow velocity (m/s)
W	Relative flow velocity (m/s)
Z	Section modulus of the blade (m^3)
θ	Azimuth angle (°)
μ	Dynamic viscosity (Pa s)
μ_t	Turbulent viscosity (Pa s)
ρ	Density (kg/m^3)
σ	Solidity (-)
σ_b	Bending stress (Pa)
τ	Shear stress (Pa)
ν	Kinematic viscosity (m^2/s)
ω	Turbulence specific dissipation rate (1/s)
ω_T	Angular velocity (rad/s)

APPENDIX A: GOVERNING EQUATIONS FOR FLUID MODELING

The Navier–Stokes equations describe a set of partial differential equations that are the governing equations in fluid mechanics needed to calculate the flow fields in this study. These equations are based on mass, momentum, and energy conservation. For the case of an isothermal flow, only the mass and momentum conservation needs to be taken into account. For an incompressible (density $\rho =$ constant) Newtonian fluid with a constant dynamic viscosity μ this results in Eqs. (A1) and (A2), where V is the velocity, g is the acceleration, and p is the pressure.

$$\frac{\partial V_i}{\partial x_i} = 0, \tag{A1}$$

$$\rho\left(\frac{\partial V_j}{\partial t} + V_i\frac{\partial V_j}{\partial x_i}\right) = -\frac{\partial p}{\partial x_j} + \mu\frac{\partial^2 V_j}{\partial x_i \partial x_i} + \rho g_j. \tag{A2}$$

The direct solving of these equations is possible using the direct numerical simulation (DNS) method. It is, however, computationally demanding due to the necessity of a very fine mesh and an extremely small time step. An alternative possibility is to simplify the equations by time-averaging the flow properties, which leads to the unsteady Reynolds-averaged Navier–Stokes (URANS) formulation given in Eqs. (A3) and (A4).

$$\frac{\partial \overline{V}_i}{\partial x_i} = 0, \tag{A3}$$

$$\rho\left(\frac{\partial \overline{V}_j}{\partial t}+\overline{V}_i\frac{\partial \overline{V}_j}{\partial x_i}\right)=-\frac{\partial \overline{p}}{\partial x_j}+\mu\frac{\partial^2 \overline{V}_j}{\partial x_i \partial x_i}-\frac{\partial}{\partial x_i}\left(\rho\overline{V_i' V_j'}\right)+\rho g_j. \tag{A4}$$

It can be seen that in Eq. (A4), a new term ($\rho\overline{V_i' V_j'}$) appears, which takes into account turbulent fluctuations. This term is known as the Reynolds stress tensor, and solving it would introduce six new unknowns into the equation system. In order to close the system, a turbulence model is required. Most of these work by expressing the Reynolds stress tensor based on the eddy-viscosity (Boussinesq) hypothesis, as shown in Eq. (A5), where μ_t and ν_t are the dynamic and kinematic turbulence viscosity, respectively, and k is the turbulent kinetic energy.

$$-\rho\overline{V_i' V_j'}=\mu_t\left(\frac{\partial \overline{V}_i}{\partial x_j}+\frac{\partial \overline{V}_j}{\partial x_i}\right)-\frac{2}{3}\rho k\,\delta_{ij}\quad\text{with }\mu_t=\rho\nu_t. \tag{A5}$$

In the present study, Menters k–ω–SST turbulence model is applied,[51] which combines the k–ω and the k–ε model. The kinematic turbulence viscosity can be solved following Eq. (A6), where a_1 is a model constant, ω is the specific dissipation rate, S is the invariant of the mean strain-rate tensor, and F_2 is a blending function.

$$\nu_t=\frac{a_1 k}{\max(a_1\omega;\, S F_2)}. \tag{A6}$$

To provide closure of the Reynolds stresses the k–ω–SST turbulence model introduces two additional equations for the turbulence kinetic energy k and the specific dissipation rate ω. These are defined by Eqs. (A7) and (A8).

$$\frac{\partial(\rho k)}{\partial t}+\frac{\partial(\rho V_j k)}{\partial x_j}=\tilde{P}_k-\beta^*\rho k\omega+\frac{\partial}{\partial x_j}\left[(\mu+\sigma_k\mu_t)\frac{\partial k}{\partial x_j}\right], \tag{A7}$$

$$\frac{\partial(\rho\omega)}{\partial t}+\frac{\partial(\rho V_j\omega)}{\partial x_j}=\alpha\rho S^2-\beta\rho\omega^2+\frac{\partial}{\partial x_j}\left[(\mu+\sigma_\omega\mu_t)\frac{\partial\omega}{\partial x_j}\right]+2(1-F_1)\rho\sigma_{\omega2}\frac{1}{\omega}\frac{\partial k}{\partial x_j}\frac{\partial\omega}{\partial x_j}. \tag{A8}$$

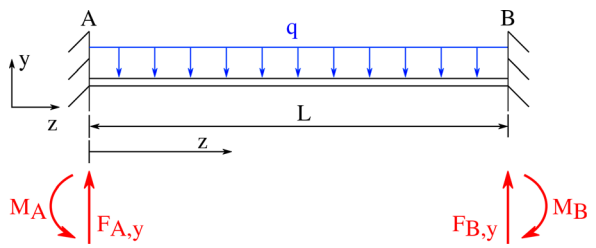

FIG. 14. Schematic representation of the fixed beam with an evenly distributed load q over the span of the blade. Forces and moments acting on the supports are presented in red. Adapted from Ruiz-Hussmann *et al.*, Int. Mar. Energy J. **8**, 47–55 (2025).[47] Copyright 2025 Author(s), licensed under a Creative Commons Attribution (CC BY) license.

In these equations α, β, β^*, σ_k, σ_ω, and $\sigma_{\omega2}$ are model constants, F_1 is a blending function, and $\tilde{P}_k$ denotes the production of turbulent kinetic energy. More information can be found in Menter *et al.*[51]

APPENDIX B: GOVERNING EQUATIONS OF THE EULER–BERNOULLI BEAM THEORY

In the present study, the Euler–Bernoulli beam theory is applied to determine the response of the blade to the applied loads. This model uses the basic equations of continuum mechanics. This theory considers the cross-sectional plane of the beam, in our case the blade, to stay perpendicular to the beam axis after deformation. In addition, the cross section is assumed to stay flat and unwarped after bending. Furthermore, in the EBB theory, the deformation occurs only from normal forces, which are applied linearly over the beam's cross section, while shear deformation and shear stresses are neglected.[70]

The EBB theory links the load acting on the beam with the deflection through Eq. (B1), stating that the fourth derivative of the deflection v is proportional to the applied load q. E is the Young's modulus and I is the second moment of area.

$$EI\frac{\mathrm{d}^4 v(z)}{\mathrm{d}z^4}=q(z). \tag{B1}$$

Derivation of this equation results in the following relationship between the internal Moment $M(z)$ and the deflection.

$$EI\frac{\mathrm{d}^2 v(z)}{\mathrm{d}z^2}=M(z). \tag{B2}$$

In the present study is modeled as a beam that is fixed at both ends with an evenly distributed load acting over the span of the blade. Figure 14 shows a schematic representation, where the forces and moments acting on the supports are shown in red.

The forces and moments on the supports need to be solved in order to determine the internal forces that cause bending stresses in the blades. Together with the presented equations, the equilibrium relations for forces and moments, and the boundary conditions for the present case [see Eq. (B3)], the support reactions are calculated.

$$v(0)=v(L)=0\quad\text{and}\quad v'(0)=v'(L)=0. \tag{B3}$$

APPENDIX C: DETAILS OF THE MESH SENSITIVITY STUDY

A grid sensitivity study in two steps was carried out to find the optimal grid size, which gives correct results while reducing time and numerical resources for each simulation. In the present case, the turbine power coefficient C_P was chosen as the reference metric. The calculation of this value is further explained in Sec. II C 1. The results of the average C_P value where compared between the different mesh sizes, taking the finest mesh as reference. The grid sensitivity study was ran for 11 revolutions using the reference blade shape (cambered NACA0018, chord length 72.44 mm) at a TSR = 2.25 and the same boundary conditions described in Sec. II B 2. At first, the mesh of the blade sub-domain was kept equal while the mesh of the fixed sub-domains (shown in blue in Fig. 4)

TABLE VIII. Details of the meshes generated as part of the two step grid sensitivity study. For the meshes 1–5 the blade disk domain was kept constant, for the meshes 4 and 6–9 the fixed domain of mesh 4 was employed, and the cells in the blade domain were modified by changing the number of cells around and perpendicular to the blade.

	Cells				
Mesh	Total	Fixed domain	Blade domain	Around blade	Perpendicular to blade
1	497 362	381 532	38 610	297	130
2	209 842	94 012	38 610	297	130
3	177 530	61 700	38 610	297	130
4	157 965	42 135	38 610	297	130
5	139 735	23 905	38 610	297	130
6	131 235	42 135	29 700	297	100
7	120 975	42 135	26 280	219	120
8	107 835	42 135	21 900	219	100
9	88 965	42 135	15 610	223	70

TABLE IX. Power coefficients obtained with the different meshes and their percentage deviation compared to the finest mesh of the respective study.

	Mesh	Total cells	Average C_P	C_P variation	CPU time
Constant blade domain	1	497 362	0.308	⋯	285 h
	2	209 842	0.306	0.51%	123 h
	3	177 530	0.306	0.69%	95 h
	4	157 965	0.305	0.96%	80 h
	5	139 735	0.298	3.0%	67 h
Constant fixed domain	4	157 965	0.305	⋯	80 h
	6	131 235	0.296	2.99%	72 h
	7	120 975	0.305	0.06%	72 h
	8	107 835	0.294	3.46%	65 h
	9	88 965	0.298	2.37%	53 h

TABLE X. Power coefficients obtained with the different time steps and their percentage deviation compared to smallest time step.

	Time step	Average C_P	C_P variation	CPU time
TSR = 1.5	0.25°	0.245	⋯	319 h
	0.5°	0.261	6.7%	167 h
	1.0°	0.275	12.3%	99 h
	2.0°	0.294	20.2%	53 h
	4.0°	0.251	2.54%	26 h
	8.0°	0.221	9.69%	14 h
TSR = 2.25	0.25°	0.294	⋯	322 h
	0.5°	0.299	1.53%	193 h
	1.0°	0.295	0.23%	96 h
	2.0°	0.298	1.29%	58 h
	4.0°	0.301	2.30%	27 h
	8.0°	0.251	14.7%	15 h

was refined. After finding the most suitable mesh of the fixed region, the mesh of the blade sub-domain was adapted. Splitting up the mesh sensitivity analysis into two steps ensures a resolved boundary layer close to the blade walls during the complete analysis.

For the first step, five different meshes (meshes 1–5) were generated with different cell sizes for the fixed domain. The mesh of the three blade disks was kept equal with 38 600 cells each, making sure to keep a $y^+ \sim 1$ close to the blades. Table VIII lists the details of the different meshes generated, and Table IX shows the average C_P value during the final revolution and the percentage deviation compared to the finest mesh. Among the five meshes generated in the first step, meshes 1 through 4 produced similar C_P values, with deviations of less than 1% from the finest mesh. Therefore, mesh 4 was selected for the fixed domain as it represents the best compromise between accuracy and computational efficiency.

In the following step, mesh 4 is taken as the reference mesh and only the cells in the blade domain are adapted, so the fixed domain remains constant. For this purpose, the number of cells around the blade and perpendicular to the blade are modified in several steps, leading to five different meshes (mesh 4 and 6–9). By adapting the cell refinement in the domain, it was made sure to always keep $y^+ \sim 1$ close to the blade. The exact number of cells around and perpendicular to the blade can be taken from Table VIII. In Table IX it can be seen, that by reducing the amount of cells around the blade, the average C_P value strongly deviates from the reference value. Mesh 7 has been chosen as the final mesh, as it has a very low deviation.

APPENDIX D: DETAILS OF THE TIME STEP SENSITIVITY STUDY

Additional to the grid sensitivity study, a time sensitivity study has been conducted. In this study, the accuracy of the simulations was examined as a function of the time step. For this purpose, the reference case (cambered NACA0018, $c = 72.44$ mm) was simulated using six different time steps corresponding to the variation of the turbine's azimuth angle of 8°, 4°, 2°, 1°, 0.5°, and 0.25°. This was conducted for two different operating points: a TSR of 2.25 and 1.5,

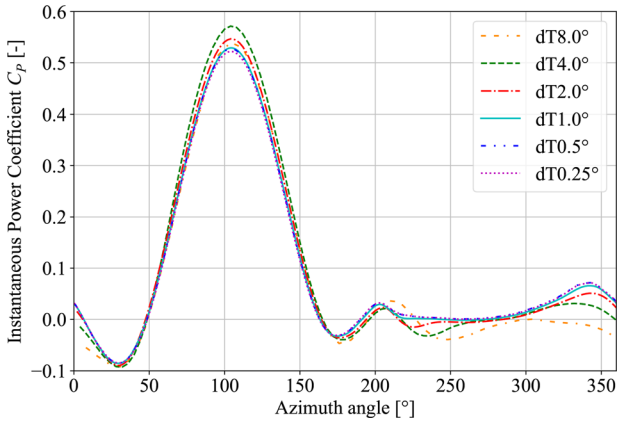

FIG. 15. Instantaneous power coefficients C_P curves for one blade obtained with the different time steps during the tenth simulated revolution. The studied case corresponds to the reference case (cambered NACA0018, $c = 72.44$ mm) at a TSR equal to 2.25.

the latter being the most challenging TSR that might be faced in the present study. Again, the average turbine power coefficient C_P was chosen as the reference metric taking the value of the smallest time step as the reference. Table X shows the results of the average C_P and its percentage deviation compared to the smallest time step for the two tested TSR. For a TSR of 1.5 it can be seen that the average C_P fluctuates between the different time steps, while for a TSR of 2.25, the error increases with an increasing time step.

In addition to the average turbine power coefficient C_P, the instantaneous C_P for one blade over the last simulated revolution was considered. The obtained curves for the different time steps are shown in Fig. 15 for a TSR equal to 2.25. It can be seen that from a time step corresponding to 1° the curve progression is very similar to the smaller time steps. Therefore, it can be concluded that the instantaneous C_P is well predicted starting at a time step corresponding to a 1° change of the azimuth angle.

For this reason, a time step corresponding to the variation of the turbines azimuth angle of 1° has been chosen. It well predicts the instantaneous C_P trend and is a trade-off between the accuracy (percentage deviation lower than 1% for a TSR of 2.25) and the computational time, which is much lower than for the smaller time steps.

REFERENCES

[1]R. W. Whittlesey, S. Liska, and J. O. Dabiri, "Fish schooling as a basis for vertical axis wind turbine farm design," Bioinspiration Biomimetics **5**, 035005 (2010).
[2]J. O. Dabiri, "Potential order-of-magnitude enhancement of wind farm power density via counter-rotating vertical-axis wind turbine arrays," J. Renewable Sustainable Energy **3**, 043104 (2011).
[3]I. D. Brownstein, M. Kinzel, and J. O. Dabiri, "Performance enhancement of downstream vertical-axis wind turbines," J. Renewable Sustainable Energy **8**, 053306 (2016).
[4]P.-L. Delafin, F. Deniset, J. A. Astolfi, and F. Hauville, "Performance improvement of a Darrieus tidal turbine with active variable pitch," Energies **14**, 667 (2021).
[5]S. Hoerner, S. Abbaszadeh, O. Cleynen, C. Bonamy, T. Maître, and D. Thévenin, "Passive flow control mechanisms with bioinspired flexible blades in cross-flow tidal turbines," Exp. Fluids **62**, 104 (2021).
[6]B. Kirke, "Tests on ducted and bare helical and straight blade Darrieus hydrokinetic turbines," Renewable Energy **36**, 3013–3022 (2011).
[7]B. Kirke and L. Lazauskas, "Limitations of fixed pitch Darrieus hydrokinetic turbines and the challenge of variable pitch," Renewable Energy **36**, 893–897 (2011).
[8]S. Abbaszadeh, S. Hoerner, T. Maître, and R. Leidhold, "Experimental investigation of an optimised pitch control for a vertical-axis turbine," IET Renewable Power Gener. **13**, 3106–3112 (2019).
[9]M. Khan, G. Bhuyan, M. Iqbal, and J. Quaicoe, "Hydrokinetic energy conversion systems and assessment of horizontal and vertical axis turbines for river and tidal applications: A technology status review," Appl. Energy **86**, 1823–1835 (2009).
[10]F. Balduzzi, P. F. Melani, G. Soraperra, A. Brighenti, L. Battisti, and A. Bianchini, "Some design guidelines to adapt a Darrieus vertical axis turbine for use in hydrokinetic applications," E3S Web Conf. **312**, 08017 (2021).
[11]F. Geng, A. Suiker, A. Rezaeiha, H. Montazeri, and B. Blocken, "A computational framework for the lifetime prediction of vertical-axis wind turbines: CFD simulations and high-cycle fatigue modeling," Int. J. Solids Struct. **284**, 112504 (2023).
[12]P.-O. Descoteaux and M. Olivier, "Performances of vertical-axis hydrokinetic turbines with chordwise-flexible blades," J. Fluids Struct. **102**, 103235 (2021).
[13]B. Yang and X. Shu, "Hydrofoil optimization and experimental validation in helical vertical axis turbine for power generation from marine current," Ocean Eng. **42**, 35–46 (2012).
[14]A. Gharib-Yosry, E. Á. Álvarez, R. Espina-Valdés, A. Pandal, and E. Blanco-Marigorta, "Experimental and multiphase modeling of small vertical-axis hydrokinetic turbine with free-surface variations," Renewable Energy **203**, 788–801 (2023).
[15]J. Gorle, L. Chatellier, F. Pons, and M. Ba, "Flow and performance analysis of H-Darrieus hydroturbine in a confined flow: A computational and experimental study," J. Fluids Struct. **66**, 382–402 (2016).
[16]L. Lazauskas and B. Kirke, "Modeling passive variable pitch cross flow hydrokinetic turbines to maximize performance and smooth operation," Renewable Energy **45**, 41–50 (2012).
[17]A. Snortland, A. Hunt, O. Williams, and B. Polagye, "Influence of the downstream blade sweep on cross-flow turbine performance," J. Renewable Sustainable Energy **17**, 013301 (2025).
[18]A. Athair, A. Snortland, I. Scherl, B. Polagye, and O. Williams, "Intracycle control sensitivity of cross-flow turbines," in *Proceedings of the European Wave and Tidal Energy Conference* (EWTEC, 2023), Vol. 15.
[19]B. Paillard, J. Astolfi, and F. Hauville, "Uranse simulation of an active variable-pitch cross-flow Darrieus tidal turbine: Sinusoidal pitch function investigation," Int. J. Mar. Energy **11**, 9–26 (2015).
[20]I. Ali, S. Khan Baloch, S. Samo, and T. Hussain, "Stress and fatigue life prediction of the H-type Darrieus vertical axis turbine for micro-hydropower applications," J. Mech. Contin. Math. Sci. **16**, 28–38 (2021).
[21]T. Bennecke, K. Ruiz Hussmann, P. Joedecke, C.-T. Weber, P.-L. Delafin, C. Bonamy, and S. Hoerner, "A weak coupled model for the fluid-structure interactions on cross-flow tidal turbine model," in ECCOMAS Congress, Oslo, Norway (2022).
[22]E. Gorgun, "Numerical analysis of inflow turbulence intensity impact on the stress and fatigue life of vertical axis hydrokinetic turbine," Phys. Fluids **36**, 015111 (2024).
[23]M. Ari, Y. S. Hadiwidodo, and M. Mukhtasor, "Evaluating mechanical strength in vertical-axis tidal turbines: A comparative study of internal blade structure and material selection through CFD simulation," in *E3S Web of Conferences* (EDP Sciences, 2024), Vol. 473, p. 03004.
[24]M. Badshah, S. Badshah, J. VanZwieten, S. Jan, M. Amir, and S. A. Malik, "Coupled fluid-structure interaction modelling of loads variation and fatigue life of a full-scale tidal turbine under the effect of velocity profile," Energies **12**, 2217 (2019).
[25]W. Finnegan, E. Fagan, T. Flanagan, A. Doyle, and J. Goggins, "Operational fatigue loading on tidal turbine blades using computational fluid dynamics," Renewable Energy **152**, 430–440 (2020).
[26]S. de Souza Custódio Filho, H. M. Santana, J. R. P. Vaz, L. D. Rodrigues, and A. L. A. Mesquita, "Fatigue life estimation of hydrokinetic turbine blades," J. Braz. Soc. Mech. Sci. Eng. **42**, 281 (2020).
[27]H. Gonabadi, A. Oila, A. Yadav, and S. Bull, "Fatigue life prediction of composite tidal turbine blades," Ocean Eng. **260**, 111903 (2022).

[28]Y. Zhang, Z. Liu, C. Li, X. Wang, Y. Zheng, Z. Zhang, E. Fernandez-Rodriguez, and R. J. Mahfoud, "Fluid–structure interaction modeling of structural loads and fatigue life analysis of tidal stream turbine," Mathematics **10**, 3674 (2022).
[29]S. Walker and P. Thies, "A review of component and system reliability in tidal turbine deployments," Renewable Sustainable Energy Rev. **151**, 111495 (2021).
[30]R. Saeed, A. Galybin, and V. Popov, "Modelling of flow-induced stresses in a Francis turbine runner," Adv. Eng. Software **41**, 1245–1255 (2010).
[31]M. Sick, W. Michler, T. Weiss, and H. Keck, "Recent developments in the dynamic analysis of water turbines," Proc. Inst. Mech. Eng., Part A **223**, 415–427 (2009).
[32]L. Andolfatto, M. Rentschler, W. Haeussler, and N. Gervais, "Opening sequence optimization for La Coche pumps back-to-back start-up through electrically coupled Pelton unit," IOP Conf. Ser. **774**, 012067 (2021).
[33]D. Kumar and S. Sarkar, "Numerical investigation of hydraulic load and stress induced in Savonius hydrokinetic turbine with the effects of augmentation techniques through fluid-structure interaction analysis," Energy **116**, 609–618 (2016).
[34]J. Lin, Y.-L. Xu, and Y. Xia, "Structural analysis of large-scale vertical axis wind turbines Part II: Fatigue and ultimate strength analyses," Energies **12**, 2584 (2019).
[35]M. S. Hameed and S. K. Afaq, "Design and analysis of a straight bladed vertical axis wind turbine blade using analytical and numerical techniques," Ocean Eng. **57**, 248–255 (2013).
[36]A. Alerci, E. Vagnoni, and M. Paolone, "Structural impact of the start-up sequence on Pelton turbines lifetime: Analytical prediction and polynomial optimization," Renewable Energy **218**, 119341 (2023).
[37]E. P. G. Putini and F. d. A. Silva, "Fatigue life estimation in a hydrogenerator rotor with cracks using the finite element method," J. Braz. Soc. Mech. Sci. Eng. **40**, 429 (2018).
[38]M. Seydoux, E. Vagnoni, C. Nicolet, and M. Paolone, "On the prediction of the induced damage by the start-up sequence of Francis turbines: On operational resilience framework," Renewable Energy **228**, 120587 (2024).
[39]K. O. Ronold, J. Wedel-Heinen, and C. J. Christensen, "Reliability-based fatigue design of wind-turbine rotor blades," Eng. Struct. **21**, 1101–1114 (1999).
[40]C. Bierögel and W. Grellmann, "Fatigue loading of plastics—Introduction," in *Polymer Solids and Polymer Melts—Mechanical and Thermomechanical Properties of Polymers* (Springer Berlin Heidelberg, 2014), pp. 281–286.
[41]S. Pessel and M. Mensinger, "Fracture mechanics based approach to the significance of certain loads on the service life of rails," Transp. Res. Procedia **14**, 2006–2014 (2016).
[42]D. Jelaska, S. Glodež, and S. Podrug, *Closed Form Expression for Fatigue Life Prediction at Combined HCF/LCF Loading* (Facta Universitatis, 2003).
[43]L. MatWeb, see https://asm.matweb.com/search/specificmaterial.asp?bassnum=mq304a for "AISI Type 304 Stainless Steel" (last accessed September 16, 2025).
[44]L. MatWeb, see https://asm.matweb.com/search/specificmaterial.asp?bassnum=ma6061t6 for "Aluminum 6061-T6; 6061-T651" (last accessed September 16, 2025).
[45]Formlabs, see https://formlabs.com/de/shop/materials/clear-resin-v4-1/?srsltid=AfmBOoo0DQzLmyVT13qvmVg__9Ba6ldCe3hLRaYeJhtcqTl4tr2UBdic for "Clear Resin V4.1" (last accessed September 16, 2025).
[46]I. Sobol, "On the distribution of points in a cube and the approximate evaluation of integrals," USSR Comput. Math. Math. Phys. **7**, 86–112 (1967).
[47]K. Ruiz-Hussmann, P.-L. Delafin, C. Bonamy, Y. Delannoy, D. Thévenin, and S. Hoerner, "Objective functions for the blade shape optimisation of a cross-flow tidal turbine under constraints," Int. J. Mar. Eng. **8**, 47–55 (2025).
[48]M. Shiono, K. Suzuki, and S. Kiho, "An experimental study of the characteristics of a Darrieus turbine for tidal power generation," Electr. Eng. Jpn. **132**, 38–47 (2000).
[49]T. Maître, E. Amet, and C. Pellone, "Modeling of the flow in a Darrieus water turbine: Wall grid refinement analysis and comparison with experiments," Renewable Energy **51**, 497–512 (2013).
[50]P. Dierckx, "Algorithms for smoothing data with periodic and parametric splines," Comput. Graph. Image Process. **20**, 171–184 (1982).
[51]F. R. Menter, M. Kuntz, R. Langtry *et al.*, "Ten years of industrial experience with the SST turbulence model," Turbul., Heat Mass Transfer **4**, 625–632 (2003).
[52]A. Bianchini, F. Balduzzi, P. Bachant, G. Ferrara, and L. Ferrari, "Effectiveness of two-dimensional CFD simulations for Darrieus VAWT: A combined numerical and experimental assessment," Energy Convers. Manage. **136**, 318–328 (2017).
[53]V. Clary, T. Oudart, P. Larroudé, J. Sommeria, and T. Maître, "An optimally-controlled rans actuator force model for efficient computations of tidal turbine arrays," Ocean Eng. **212**, 107677 (2020).
[54]M. Dave and J. A. Franck, "Comparison of RANS and LES for a cross-flow turbine in confined and unconfined flow," J. Renewable Sustainable Energy **13**, 064503 (2021).
[55]S. Hoerner, S. Abbaszadeh, T. Maître, O. Cleynen, and D. Thévenin, "Characteristics of the fluid–structure interaction within Darrieus water turbines with highly flexible blades," J. Fluids Struct. **88**, 13–30 (2019).
[56]C. Bonamy, J. Chauchat, P. Augier, A. Mathieu, Q. Clemencot, R. Chassagne, G. Maurice, A. Gilletta, M. Renaud, and G. Gonçalves (2022). "fluiddyn/fluidfoam: Release v0.2.3," Zenodo. https://doi.org/10.5281/zenodo.6453090
[57]A. Luévanos-Rojas and J. Montoya-Ramírez, "Mathematical model for rectangular beams of variable cross section of symmetrical linear shape for uniformly distributed load," Int. J. Innovative Comput., Inf. Control **10**, 545–564 (2014).
[58]T. Bennecke, K. Ruiz-Hussmann, P. Joedecke, S. Abbaszadeh, P.-L. Delafin, C.-T. Weber, and S. Hoerner, "Methodology to capture the single blade loads on a cross-flow tidal turbine flume model," in *Proceedings of the European Wave and Tidal Energy Conference* (EWTEC, 2023), Vol. 15.
[59]G. Niemann, H. Winter, B.-R. Höhn, and K. Stahl, *Maschinenelemente 1: Konstruktion Und Berechnung Von Verbindungen, Lagern, Wellen* (Springer Berlin Heidelberg, 2019).
[60]*Handbuch Maschinenbau*, edited by A. Böge and W. Böge (Springer Fachmedien Wiesbaden, 2021).
[61]H. Wittel, D. Muhs, D. Jannasch, and J. Voßiek, *Roloff/Matek Maschinenelemente: Normung, Berechnung, Gestaltung* (Springer Fachmedien Wiesbaden, 2015).
[62]Y. Li and S. M. Calisal, "Three-dimensional effects and arm effects on modeling a vertical axis tidal current turbine," Renewable Energy **35**, 2325–2334 (2010).
[63]R. Gosselin, G. Dumas, and M. Boudreau, "Parametric study of H-Darrieus vertical-axis turbines using CFD simulations," J. Renewable Sustainable Energy **8**, 053301 (2016).
[64]C. Li, S. Zhu, Y.-L. Xu, and Y. Xiao, "2.5D large eddy simulation of vertical axis wind turbine in consideration of high angle of attack flow," Renewable Energy **51**, 317–330 (2013).
[65]P. Bachant and M. Wosnik, "Modeling the near-wake of a vertical-axis cross-flow turbine with 2-D and 3-D RANS," J. Renewable Sustainable Energy **8**, 053311 (2016).
[66]W. Liu and Q. Xiao, "Investigation on Darrieus type straight blade vertical axis wind turbine with flexible blade," Ocean Eng. **110**, 339–356 (2015).
[67]W. Liu, Q. Xiao, and F. Cheng, "A bio-inspired study on tidal energy extraction with flexible flapping wings," Bioinspiration Biomimetics **8**, 036011 (2013).
[68]E. Sansone, C. Pellone, and T. Maitre, "Modeling the unsteady cavitating flow in a cross-flow water turbine," J. Fluids Eng. **132**, 071302 (2010).
[69]F. Alqurashi and M. H. Mohamed, "Aerodynamic forces affecting the H-rotor Darrieus wind turbine," Modell. Simul. Eng. **2020**, 1–15.
[70]A. Öchsner, *Classical Beam Theories of Structural Mechanics* (Springer International Publishing, 2021).